Westfälische
Wilhelms-Universität
Münster

Universidad de
Sevilla

Master's Thesis

Test setup for a fluorescence detector to be used in the laser cooling system at the new SIS100 accelerator at GSI

Lucas Garrido Gómez

supervised by
Dr. Volker Hannen

5th February 2021

Referent: Prof. Dr. Christian Weinheimer,
from Westfäliche Wilhelms-Universität Münster

Correferent: Prof. Dr. Manuel García-León,
from Universidad de Sevilla

Declaration of Academic Integrity

I hereby confirm that this thesis on

Test setup for a fluorescence detector to be used in the laser cooling system at the new SIS100 accelerator at GSI

is solely my own work and that I have used no sources or aids other than the ones stated. All passages in my thesis for which other sources, including electronic media, have been used, be it direct quotes or content references, have been acknowledged as such and the sources have been cited.

I agree to have my thesis checked in order to rule out potential similarities with other works and to have my thesis stored in a database for this purpose.

Signature: 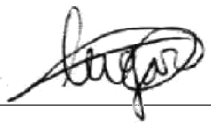

Your comfort zone will kill you.

— Random Instagram post

Contents

Acknowledgements

I would like to express my deepest gratitude to Christian Weinheimer for letting me be part of this group. I am also extremely grateful to Volker Hannen for being an outstanding supervisor. You have both been very good advisors and I have learned countless, valuable things from you. I would like to extend my sincere thanks to Alexander Kappes and Joaquín Ramírez Rico, who have always been concerned that we feel comfortable throughout our stay in Germany.

This work would not have been possible without the support of Ken Ueberholz. We have been working together in both the laboratory and the office and I owe you most of these results. Thank you very much for being a great colleague.

Many thanks to Simon, Axel, Kevin, Lutz, and all the other group members who have always been there to lend a hand when I needed it. I really appreciate that.

The mechanical and electronic workshops also played a decisive role during the development of my thesis. Thanks to both teams for their useful contributions, and special thanks to the engineering crew in my corridor: Christian Huhmann, Hans-Werner Ortjohann, Lukas Wahmes, and Daniel Bonaventura. You guys do a great job.

I would like to give thanks to everybody I have met here in Münster, despite the pandemic situation we've managed to have a year full of fun.

No puedo terminar los agradecimientos sin nombrar a Dani, Fernando y Pablo, que tomaron conmigo la iniciativa de venir a pasar un año en Alemania. Ahora creo que es una de las mejores decisiones que he podido tomar en mi vida. Gracias por todos los momentos que hemos vivido juntos. Y por último, gracias a mi padre, a mi madre y a mis hermanos, porque os debo todo lo que hoy soy.

Abstract

This work deals with the design, development, and trial of a test setup for a spectrometer for the laser cooling system that will be used in the future SIS100 accelerator at GSI. First, laser cooling in the GSI/FAIR facilities is presented. Here, a detector is needed for diagnosis. If it would allow for an energy-resolved detection, measurements about the fine structure transitions in heavy ions could be performed at SIS100. To achieve this, an MCP detector is combined with a delay line anode and a diffraction grating. After introducing some basic x-ray physics, the main components of the spectrometer are discussed.

Then, the test setup that has been built in the *Institut für Kernphysik* in Münster is presented. Several tests are performed in order to check the position sensitivity and the time response of the detector. After that, the position of the entrance slit and the grating is optimized. Lastly, an energy calibration is performed and two spectra are acquired: one with a magnesium anode and one with a copper-nickel anode. The thesis concludes with a discussion about the results obtained and the outlook of the project.

Chapter 1

Introduction

In the search for knowledge of everything that surrounds us — from the small particles that shape our body to the vast dimensions of the cosmos — humans attempt to experiment to better understand how nature works. At the same time, what began as curiosity ends up generating technological developments and applications to daily life, improving our quality of life. In essence, it is through scientific research that progress is made.

That is precisely the aim at GSI (*Gesellschaft für Schwerionenforschung*), a worldwide leading accelerator facility: to reach a better understanding of the structure and behavior of matter. Furthermore, FAIR (*Facility for Antiproton and Ion Research*) is being built as an extension of GSI. At FAIR, we will be able to recreate the extreme conditions to which matter is subject in stars, giant planets, and stellar explosions. Research here is divided into four experiment pillars:

- NUSTAR — Nuclear Structure Astrophysics and Reactions. Studies on exotic nuclei help us to gain insight into how heavy elements are created.
- CBM — Compressed Baryonic Matter. The collision of atomic nuclei at high speed can simulate the conditions during the big-bang or inside supermassive objects like neutron stars.
- PANDA — Antiproton Annihilation at Darmstadt. Experiments for a better understanding of the strong force.
- APPA — Atomic, Plasma Physics and Applications. Investigation of fundamental processes in atoms and macroscopic effects in materials or tissues.

To achieve this, FAIR will have the ability to produce beams of stable and radioactive

ions, as well as antiprotons. This will be possible due to the accelerator located at the heart of the facility, the SIS100. With its 1100 meters circumference, this synchrotron-type accelerator will speed up particles to 99% of the speed of light. There will also be additional storage rings and experimental stations, and the existing facility of GSI will serve as the injector for FAIR. This thesis focuses on the development of a test setup for a spectrometer detector to be used in the laser cooling system of SIS100.

Chapter 2

Theoretical background

This chapter provides the theoretical aspects needed to understand the design of the energy-resolved fluorescence detector for the laser cooling facility at SIS100. It covers topcis from the operation of the GSI/FAIR facilities to the working principles of the different elements used to compose the spectrometer.

2.1 The FAIR facility

The *Facility for Antiproton and Ion Research* will be one of the largest and most complex accelerator facilities in the world. The construction began in the summer of 2017 as an expansion of the existing *GSI Helmholtz Centre for Heavy Ion Research*. Commissioning is planned for 2025.[1]

FAIR opens up a new world of possibilities for scientific research: it will allow to accelerate ions of all the natural elements[2] in the periodic table to almost the speed of light. The existing GSI accelerators will serve as the first acceleration stage. Beams of protons are created in the proton linear accelerator, p-LINAC, and heavy ions will be prepared in the UNILAC (*Universal Linear Accelerator*). These accelerators can speed up particles to 20% of the speed of light. Then they are injected into the SIS18 ring accelerator, which with its 216 meters circumference can accelerate ions up to 90% speed of light [1].

The future heavy-ion synchrotron SIS100 is the core of the upcoming facility. Its construction is essential for the operation of FAIR and the fulfillment of the entire experimental

[1]Progress on the construction of FAIR can be checked at the following link: `https://www.gsi.de/en/researchaccelerators/fair/fair_civil_construction.htm`

[2]That is, from hydrogen to uranium.

program. With a circumference of almost 1100 meters, it will be five times as large as the SIS18. From the latter, ions will be directed to SIS100 which will speed up ions to velocities as high as 99% of the speed of light. Eventually, they can be utilized in the CBM or APPA experiments. High energetic heavy ions can also be used to produce beams of exotic nuclei for the NUSTAR experiment. This process will take place in the *Superconducting Fragment Separator* (Super-FRS). Antiproton beams can be created by leading the proton beam to a specific target. These antiprotons will be captured and cooled in the *Collector Ring* (CR). Then they are injected into the *High-Energy Storage Ring* (HESR), where they can be used within the PANDA experiment.

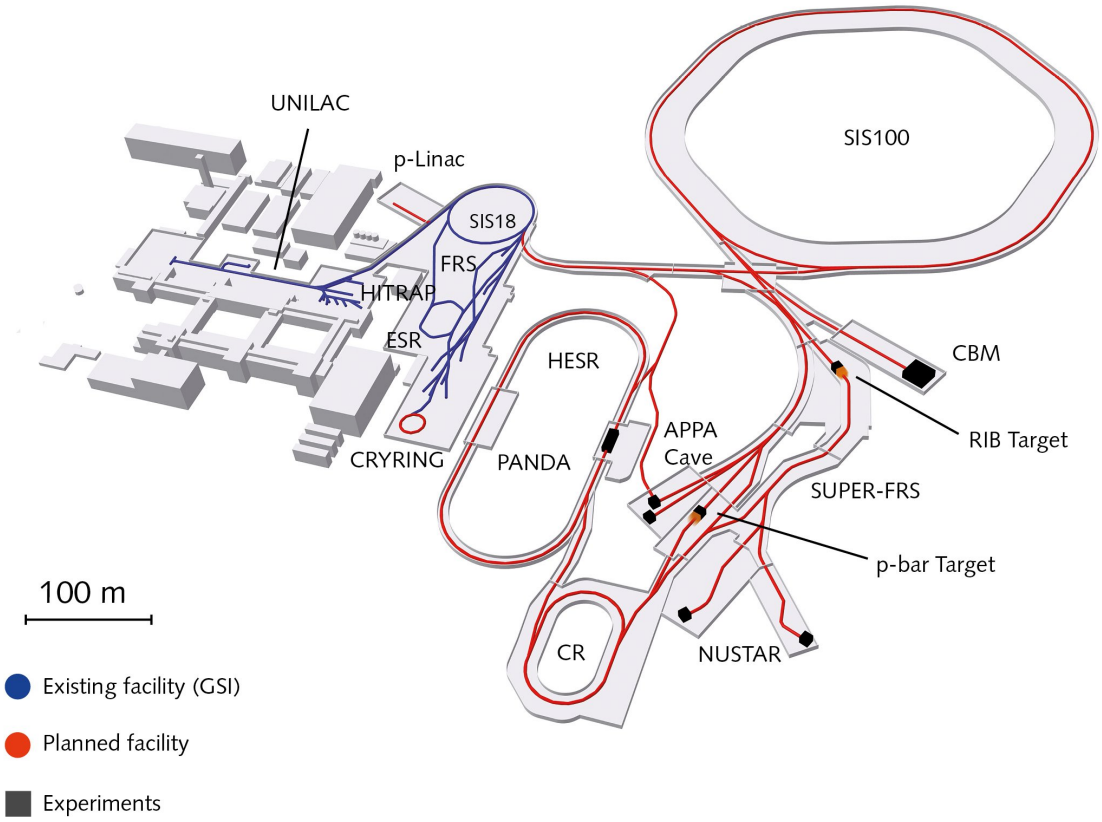

Figure 2.1: Layout of the existing GSI and the extended FAIR facility. Figure from [1].

The APPA experiment deals with the investigation of fundamental processes in atoms and their interaction in different materials or tissues. It has a wide range of applications: from the effect of cosmic rays on astronauts and spacecraft to the understanding of the interior of the earth by by bombarding minerals with high-energy ions to simulate its high pressures and temperatures. There are even plans to use FAIR to develop a cancer therapy using protons that travel at 98% of the speed of light [2].

Atomic physics research at GSI and FAIR takes place within the APPA framework. Specifically, the *Stored Particle Atomic Physics Research Collaboration* (SPARC) is using the facilities to conduct heavy ion experiments with two main goals: first, to test quantum electrodynamics in the regime of extremely strong electromagnetic fields, and second, to study atomic transitions at relativistic velocities. The large Doppler shifts experimented by photons under these conditions allow to study transitions which are otherwise not accessible with the existing laser systems.

Besides stochastic cooling, laser cooling is the only feasible method for cooling of the ion beams at SIS100. Laser cooling has already been demonstrated at the *Experimental Storage Ring* (ESR) at GSI [3], and it will be attempted for the first time with highly charged ion beams in SIS100 [4]. For these experiments, a detector is needed for photons within the extreme ultraviolet and soft x-ray range. This thesis aims to test the design of such a detector, as well as to perform the first measurements to check its performance.

2.2 Beam cooling

2.2.1 Introduction

In accelerators, particles are created in an ion source and accelerated to the desired velocity. However, since there is always a certain uncertainty in the particles' momentum, the velocities do not have a fixed value but follow a specific distribution. Due to imperfections, this distribution can get wider as it proceeds through the accelerator chain, but the demanded accuracy in experiments requires a narrow momentum distribution.

The momentum spread of a particle ensemble is closely related to its temperature T, according to the equipartition theorem:

$$\frac{3}{2}k_B T = \frac{1}{2}m\left\langle |\mathbf{v} - \langle \mathbf{v} \rangle|^2 \right\rangle \ , \tag{2.1}$$

k_B being the Boltzmann constant, m the mass of the particles, and $\mathbf{v}$ their speed. This theorem states that in thermal equilibrium, energy is distributed evenly among the three degrees of freedom. This is not the case when dealing with accelerated beams, where the velocity spread is usually different for the longitudinal and transverse coordinates. Thus, the temperature can be defined for each spatial coordinate as

$$\frac{1}{2}k_B T_i = \frac{1}{2}m\left[\left\langle v_i^2 \right\rangle - \langle v_i \rangle^2\right] \ . \tag{2.2}$$

That is why reducing the momentum spread of a particle set is called cooling. There are three major ways to achieve this[3]: electron cooling, stochastic cooling, and laser cooling.

Electron cooling requires the beam to be overlapped with a monochromatic electron beam over a specific distance. Electrons are produced continuously in an electron gun and accelerated to the desired ion velocity. In the electrons' rest frame, the ions pass through the e^- gas while performing Rutherford scattering. In a simplified picture, ions that are slower than the electrons are pushed and gain speed, and faster ions kick the electrons and lose energy. Consequently, the momentum distribution of the system is sharpened, as illustrated in **Figure 2.2**. Used electrons are constantly replaced by new, cold electrons for a proper heat transfer. More detailed information on electron cooling can be found in [5].

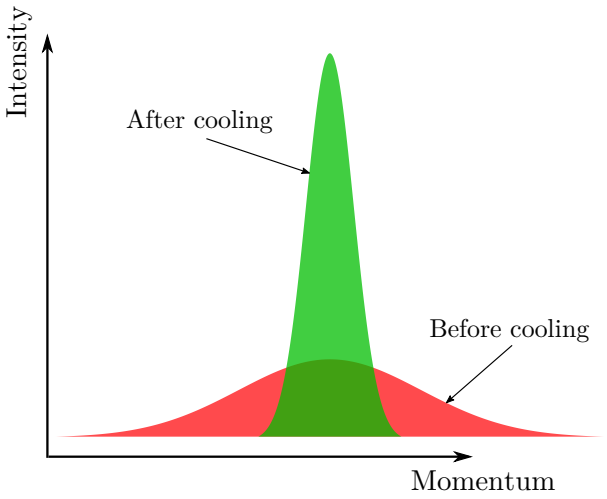

Figure 2.2: Schematic of the effect of beam cooling.

Stochastic cooling is a feedback system made of two components: a detector (pickup electrode) which measures the fluctuations of the beam and a corrector (kicker electrode) that applies the corresponding correction. This method only works for circulating beams, since the system cannot rectify the deviations in one go, but after the beam has passed through many times and a sufficient amount of time has passed. Stochastic cooling was invented by Simon van der Meer at CERN in 1972 [6], and he was awarded the Nobel Prize in Physics in 1984 for the success of this technique. Reference [7] provides a very well-explained guide on the topic.

Although these are very powerful methods whose success has been demonstrated numerous times, problems arise as the energy of the particles increases. Indeed, at relativistic speeds ($\gamma >> 1$) the efficiency of electron cooling greatly decreases, the cooler requires extreme voltages and the cooling times are excessively long [5]. On the other hand, stochastic cooling works better for low-intensity beams and also takes long times to reach the desired beam quality [8]. Then, only laser cooling remains as the most feasible choice for the future SIS100 accelerator. We will discuss this technique in more detail in the following section.

[3]More cooling methods exist, but these are the most used because of their cost and efficiency.

2.2.2 Laser cooling

Laser cooling (also called Doppler cooling[4]) is based on the excitation and deexcitation of an atomic state in the accelerated ion beam. The investigation of this cooling method was honored with the Nobel prize in 1997. William Phillips' Nobel Lecture [9] offers a great overview of the development process.

As depicted in **Figure 2.3**, an atom can absorb a photon if the energy of the latter is equal to the energy gap between two atomic levels. This energy is used to promote an electron from the ground state to a higher energy level. The excited state is not stable and the electron returns to the original state after a short time, releasing a photon in a random direction. Because of this isotropic deexcitation, the mean momentum change of these emissions is zero and the net momentum change of the atom in the whole process always points in the direction of the incident photon. Laser cooling consists of inducing this effect in the ion beam employing properly tuned lasers.

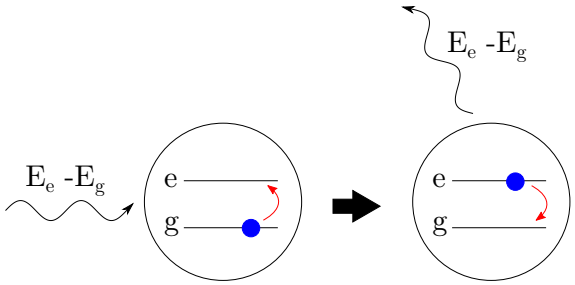

Figure 2.3: Excitation and deexcitation of an atomic state.

To achieve this, the ion beam is overlapped with a collinear and an anti-collinear laser beam. In the particle's rest frame the laser photons experience a Doppler shift: the laser coming towards the ions is shifted to shorter wavelengths (blue), and the one coming from behind is shifted to larger wavelengths (red). The co-propagating laser is tuned to excite the slowest particles, and by absorbing the photons' momentum they gain speed, on the other hand, the counter-propagating laser is tuned to excite the fastest ones, reducing their velocity in the absorptions. The net result of the process is a reduction of the momentum spread. This is illustrated in **Figure 2.4**.

In order to match the resonance condition of the atomic transition, the laser system need to satisfy the following relationships:

$$\lambda_{\text{co-}}^{(\text{lab})} = \frac{\lambda^{(\text{ion})}}{\gamma(1+\beta)} \; ; \tag{2.3a}$$

$$\lambda_{\text{counter-}}^{(\text{lab})} = \frac{\lambda^{(\text{ion})}}{\gamma(1-\beta)} \; , \tag{2.3b}$$

[4]Although the concept of laser cooling is slightly broader than Doppler cooling, it is usual that both names are used interchangeably.

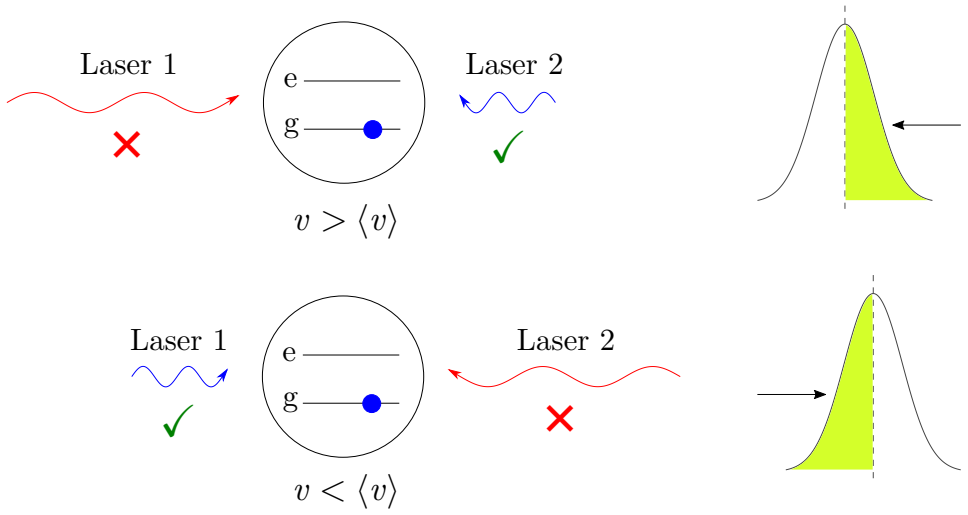

Figure 2.4: Schematic of the laser cooling process. The ion beam moves from left to right so laser 1 is the co-propagating beam and laser 2 is the counter-propagating.

where $\lambda^{(\mathrm{ion})}$ denotes the wavelength of the atomic transition in the ion rest frame and $\lambda^{(\mathrm{lab})}_{\text{co-/counter-}}$ are the needed wavelengths of the laser beams. According to the equations, the counter-propagating laser needs longer wavelengths and the co-propagating needs shorter ones for the resonance condition to be satisfied. At the very high speeds of SIS100, the Doppler shift is so strong that $\lambda^{(\mathrm{lab})}_{\text{co-}}$ becomes extremely short, and no laser systems exist (yet) which provide such small wavelengths. For example, to excite a 10 nm transition in an ion beam with $\beta = 0.95 - 0.997$ ($\gamma = 3.2 - 12.9$) one would need $\lambda^{(\mathrm{lab})}_{\text{co-}} = 0.4 - 1.6$ nm.

Several approaches have been tried to avoid using the collinear beam. An interesting way to do so is through the bunching of the ion beam, which is produced by a radio-frequency (rf) cavity. The rf cavity creates a periodic, longitudinal electric field that packs the beam into bunches and causes the ions within a bunch to perform oscillations inside a harmonic potential (called *bucket* potential). The laser beam exerts a force in the opposite direction of the ions' movement, while the restoring force of the bucket potential pushes the particles back to the center, effectively damping the oscillations and providing the co-propagating force that was needed. A more extensive study on laser cooling of bunched beams can be found in [10].

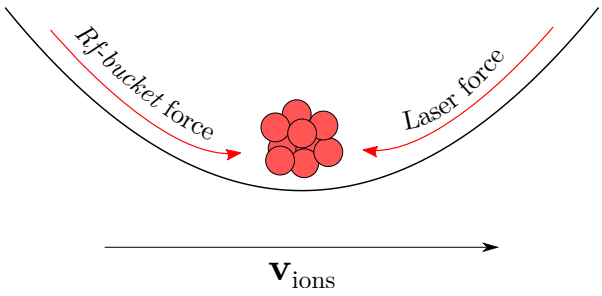

Figure 2.5: Simplified diagram showing the *bucket* potential and the two forces acting on the ion bunches.

First tests in SIS100 will be performed with lasers at two available wavelengths: 257 and 514 nm; either in pulsed or continuous wave mode [4]. With just these simple laser systems, a very wide range of ions and transitions is accessible due to the large magnetic rigidity of the accelerator. The magnetic rigidity is simply the product between the magnetic field B and the radius of curvature ρ produced by that field, and it is given by

$$B\rho = \frac{p}{q} \ . \tag{2.4}$$

Here, p and q are the momentum and the electric charge of the beam particles. SIS100 will be able to store ions with a rigidity up to 100 Tm — hence its name — while the storage ring ESR at GSI has a capacity of 10 Tm. This means that in SIS100 particles with the same charge state can be stored with a ten times higher momentum compared to ESR. Another factor that should be taken into account is the lifetime of the atomic transition. It must be much shorter than the revolution period of the ions inside the acceleration ring, as cooling takes place after a large number of absorptions and deexcitations. The ideal ones are fine structure transitions in few-electron ions.

To illustrate the flexibility of laser cooling at SIS100 it is convenient to express γ in terms of the ion properties:

$$\gamma = \sqrt{\left(\frac{B\rho q}{mc}\right)^2 + 1} \ . \tag{2.5}$$

As an example, let us consider lithium-like Sn (Sn nucleus and three electrons), which has $Z = 50$, $m \approx 119\ u$, and $q = 47\ e$. For a rigidity of 100 Tm, this leads to $\gamma \approx 13$. This means that using $\lambda^{(\mathrm{lab})} = 257$ nm, a transition of $\lambda^{(\mathrm{ion})} \approx 10$ nm can be excited, according to **Equation (2.3b)**. This corresponds to a $2s_{1/2} \rightarrow 2p_{1/2}$ transition in this ion [11]. With these simple calculations, one can see that transitions of $\lambda^{(\mathrm{ion})} = 10$ nm to 40 nm can be excited in a large variety of ions, such as the ones listed in **Table 2.1**.

Ion type	***Z***
Li-like	16–60
Be-like	14–56
B-like	7–56
Na-like	13–49

Table 2.1: Some examples of ions that can be cooled in the future SIS100.

Due to the Doppler shift, fluorescence photons coming from the deexcitations have energies from the XUV to the soft x-ray region (30 eV to 3000 eV). A detector with a fast time response and sufficient efficiency in this range would allow the diagnosis of the cooling process and also to observe the dynamics of the ion bunch inside the bucket. Having an energy-resolved detection is even more interesting since it would allow for precise spectroscopic measurements of the selected transitions.

These requirements can be met by combining a microchannel plate detector with a diffraction grating. Both devices are discussed in **Section 2.4** and **Section 2.5**, respectively.

2.3 X-ray physics

As mentioned in the previous section, we are aiming to detect photons coming from atomic deexcitations, which, due to the energy gap of the transitions in question and the Doppler shift of the wavelengths, are emitted in the x-ray regime. Before moving on to the operation of the detector, it is necessary to introduce the characteristics and behavior of this kind of electromagnetic radiation.

2.3.1 Origin and production

Characteristic x-rays are created in atoms when an electron decays from a higher shell to a lower one with a sufficiently large energy gap. In the process, a photon is emitted whose energy is exactly the difference between the two levels. This produces an emission spectrum of x-rays at discrete energies. Since atomic orbitals have different energies for each chemical element, every material has its own characteristic x-ray lines. Those transitions in which an electron decays from the upper shells to the K shell are called K lines. In the same way, electrons falling to the L shell produce L lines, and so on. If a transition comes from a level that is immediately above (e.g. L $\rightarrow$ K) the subscript α is added, if it comes from the next one (e.g. M $\rightarrow$ K) then β is added, etc. This is represented in **Figure 2.6**. Due to fine structure splitting, sometimes it is necessary to add another subscript to distinguish between levels within the same shell (e.g. $K_{\alpha 1}$, $K_{\alpha 2}$).

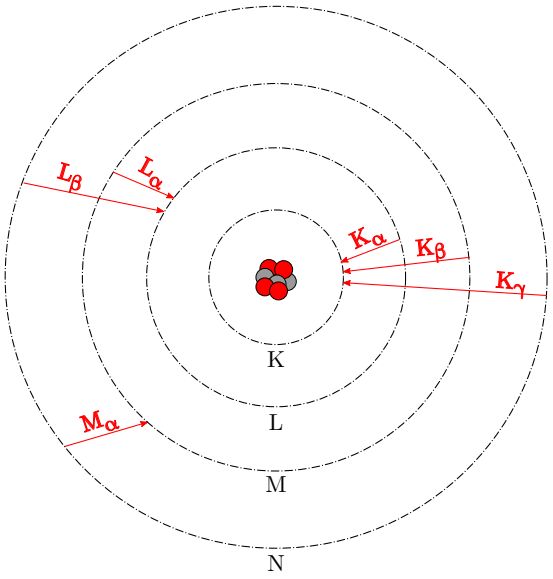

Figure 2.6: Nomenclature system for x-ray emissions.

X-rays can be generated inside a vacuum tube, using a high voltage to accelerate electrons produced by a hot cathode and leading them to a metal target, the anode. When hitting the target, they can eject an orbital electron of the anode atoms. Electrons from higher levels fill the vacancies and hence characteristic x-rays are emitted. X-ray tubes also produce a second kind of radiation when the high-velocity

electrons are deflected by the atomic nucleus. Electrons are decelerated in the process and the lost kinetic energy is converted into a photon. These x-rays have a continuous spectrum and are called braking radiation or *Bremsstrahlung*.

The maximum energy of the photons created in such a device is limited by the energy of the accelerated electrons, therefore, a 15 kV tube cannot create x-rays with an energy greater than 15 keV. In other words, the spectrum exhibits a sharp cutoff at low wavelengths at the exact value of

$$\lambda_{\text{min}} = \frac{hc}{eV} \ . \tag{2.6}$$

This formula is known as Duane-Hunt law. Hence, the typical spectrum obtained from an x-ray tube consists of a continuous bremsstrahlung curve plus the characteristic x-ray peaks at certain positions (see **Figure 2.7**). The shape of the continuous part of the spectrum is approximately described by Kramer's law [12]:

$$I(\lambda) = K \left(\frac{\lambda}{\lambda_{\text{min}}} - 1 \right) \frac{1}{\lambda^2} \ , \tag{2.7}$$

where the constant K is proportional to the atomic number of the target element.

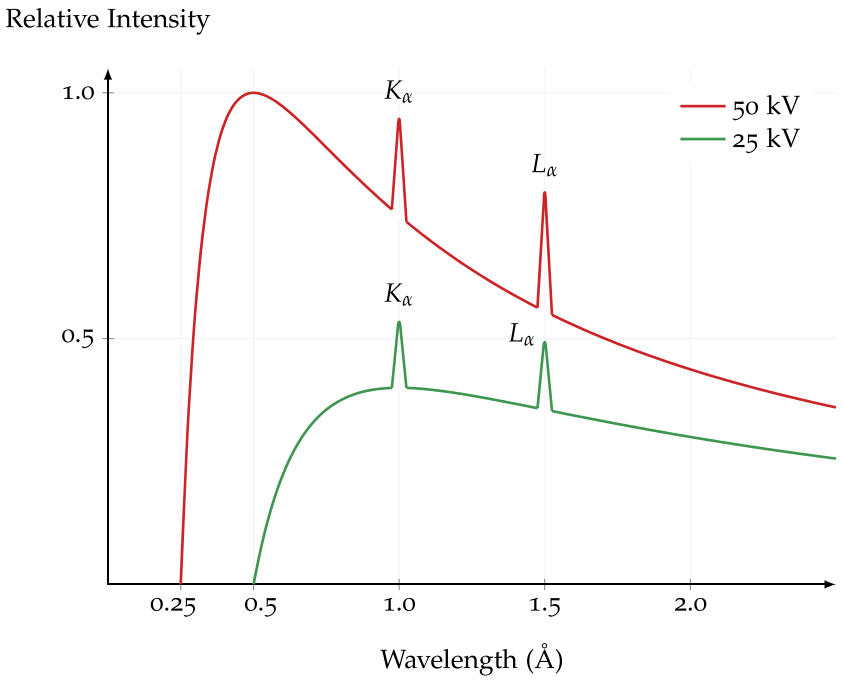

Figure 2.7: Typical spectrum obtained with an x-ray tube, showing the characteristic peaks and the bremsstrahlung. Note the variation of λ_{min} with the accelerating potential. From [13].

2.3.2 Interaction with matter

Unlike charged particles, which generally interact with matter through multiple scatterings and thus continuously losing energy, photons interact discretely. A single event can abruptly change the energy and momentum of a photon or even make it disappear. There are several mechanisms of light-matter interaction, such as photoelectric effect, Compton scattering, pair production, and photofission; but only the first one is relevant in the x-ray energy range, the others being strictly prohibited or extremely unlikely.

In the photoelectric effect, an atom absorbs a photon and ejects an electron from one of its atomic shells. As a result of the interaction, the photon completely disappears and the electron is released with an energy given by

$$E_e = h\nu - E_B \ , \tag{2.8}$$

where $h\nu$ is the energy of the incoming photon and E_B represents the binding energy of the emitted electron. If $h\nu < E_B$, the photon does not have sufficient energy to kick the electron, and the process does not take place. In most cases, the electrons are released from the most tightly bound shells of the atom (K and L). The vacancies are quickly filled through the rearrangement of electrons from other shells, and hence characteristic x-rays from the absorber element may also be created.

The photoelectric process is the predominant mechanism of interaction in the x-ray energy range. A good approximation for the probability of photoelectric absorption is given by

$$\tau \simeq \text{constant} \cdot \frac{Z^n}{E^{3.5}} \ , \tag{2.9}$$

where E is the energy of the photon, Z is the atomic number of the absorber material, and n is a number between 4 and 5 [14]. As can be seen in the formula, the process is enhanced for heavy absorbers and low energy photons. For larger energies (comparable to the electron rest mass, 511 keV), the Compton effect, which is the inelastic scattering of a photon by an electron, may take place. For even higher energies (above 1.022 MeV), pair production — creation of an electron-positron pair near a nucleus — also needs to be considered. Since these energies are beyond the x-ray range we can neglect both processes.

The elastic scattering of photons by electrons is also possible. The photon interacts with the whole atom so that it is scattered with no change in the internal energy of the scattering atom nor the x-ray photon. This process is called coherent (or Rayleigh) scattering and is the one that enable x-ray optics. However, it is often ignored because there is no energy

transfer and, moreover, the deflection angle increases at low energies, thus the scattering being mainly in the forward direction for x-rays.

2.3.3 Optical properties

The main difference between visible light and x-rays — apart from their energy — lies in the refractive index n within matter. Indeed, $n > 1$ for visible light in all materials, while in the x-ray regime the refractive indices are lower (but very close) to unity [15]. It is very common to express the refractive index as

$$n = 1 - \delta + i\beta, \tag{2.10}$$

being δ a very small, positive number. As a consequence, x-rays coming from air or vacuum and entering solids or liquids are refracted away from the normal plane of the surface (for visible light they are refracted towards the normal plane), although the difference between the two angles is very little. Besides, this fact enables total reflection at very small angles of incidence (typically called grazing incidence). The imaginary part β in (2.10) describes the attenuation of the incident rays and includes photoelectric absorption and coherent scattering. As this is very likely for x-ray beams, most materials have low reflectivity and refractivity.

There are numerous devices that can be used to manipulate an x-ray beam. These can be divided into three general categories: reflective, refractive, and diffracting elements. Reference [16] offers an exhaustive study of such devices and soft x-ray optics in general. Regarding our spectrometer for SIS100, we will use a diffraction grating to separate a polychromatic beam into its different wavelengths. This device will be studied further in **Section 2.5**.

2.4 Microchannel plate detectors

2.4.1 Operation

A microchannel plate (MCP) consists of an array of many glass capillaries which are fused together and sliced in the shape of a plate. Both faces of the disc are metalized to provide parallel electrical connections to all the capillaries. These capillaries, also called channels, work as an independent electron multiplier when a high voltage is applied between the two ends. A typical MCP has 10^5 to 10^7 channels.

MCPs can be used to detect electrons, ions, and photons. Multiple secondary electrons are emitted when a particle or a photon enters a channel from the input side and strikes

its inner wall. These electrons are accelerated by an electric field created by a voltage V_D applied across both faces of the MCP. They then strike the opposite wall in the channel, causing further secondary electrons to be emitted. This process is repeated many times along the channel and, as a result, a large number of electrons are released from the output side.

The electron cloud that leaves the MCP is collected on an anode placed behind the plate. Furthermore, as the channels form a 2D array of independent multipliers, an MCP can additionally provide spatial resolution if combined with a suitable position-sensitive anode. Even though the anode works as the detecting element, the discharging and recharging of the plate itself (produced by the e^- cascade) can be measured and used to produce a signal corresponding to a single particle or photon detection.

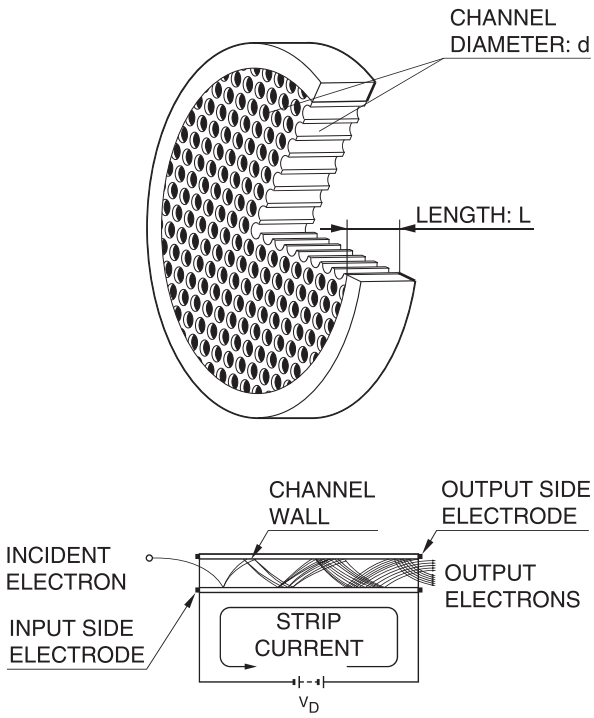

Figure 2.8: Structure and working principle of an MCP. Figure from [17].

Commonly, the channels enter the plate at a certain angle to the surface, thus ensuring that the incident radiation hits the channel wall. This angle is called the bias angle and it is chosen by taking into account different factors such as radiation type, detection efficiency, spatial resolution, etc. The optimum value usually ranges from 5 to 15 degrees.

Another important property is the Open Area Ratio (OAR), which indicates the ratio of the channel open area to the entire effective area of the MCP. Typical OAR values are between 50% and 60%. The higher this ratio is, the easier it is for the incident radiation to reach an actual channel. Custom MCPs can be manufactured with etched channel walls to increase the OAR up to 90%.

Since MCPs usually operate at a high voltage of 1kV per plate, a good vacuum is required for a proper detector operation. If operated in a poor vacuum environment, the MCP lifetime may shorten, the noise will increase due to ion generation in the channels, and in the worst cases, the plate might be damaged by discharges. To avoid this, MCPs should not be operated in a vacuum worse than $2 \cdot 10^{-6}$ mbar [17].

2.4.2 Gain and time response

The approximate gain g of an MCP is given by the following equation:

$$g = \exp(G \cdot \alpha) \ , \tag{2.11}$$

where α is the length-to-diameter ratio (L/d) and G is the gain factor of the channel walls, which is an intrinsic characteristic of the wall material. This means that different MCPs with the same α value and made of the same material will have the same gain, even if they have different sizes. Standard alpha values lie between 40 and 60.

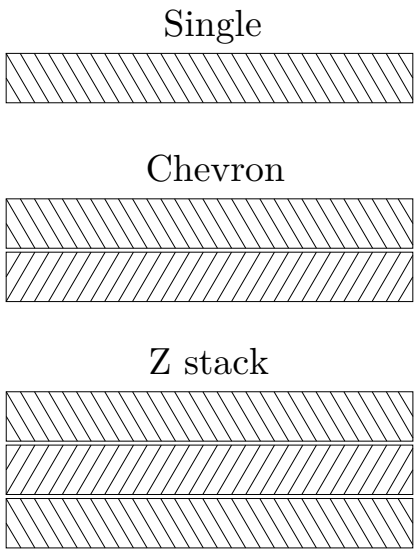

Figure 2.9: MCP configurations, showing the Chevron stack for a 2-stage MCP and the Z stack for a 3-stage one.

Gains up to 10^4 can be achieved with a single MCP. Higher gains can be reached by using two or three MCPs in stacked configurations, where the output of one plate is used as the input for the next one. The MCPs can be pressed together to preserve spatial resolution or have a small gap to spread the charge and further increase the gain. As the gain increases, the noise grows and false signals begin to show up. This happens because the secondary electrons can ionize the residual gas molecules within the channels. The positive ions then travel back to the input side of the plate, starting a new avalanche and creating false events. To reduce this ion feedback effect, it is possible to use stacked MCPs with their bias angles rotated 180 degrees, as shown in **Figure 2.9**. These configurations provide a directional change large enough to prevent the ions produced on the rear plate from reaching the front plate. With a two-stage MCP, gains higher than 10^6 can be obtained, and with a three-stage MCP higher than 10^7.

The gain of an MCP is a statistical process, and two identical particles can produce signals with different amplitudes. This leads to poor timing properties when using an ordinary discriminator due to the dependence of the trigger time on the signal's peak height. The temporal jitter resulting from this effect can be removed by using a constant fraction discriminator (see **Section 3.1.2**). Once this issue is removed, MCPs have a very high temporal resolution. The size of the MCP can be reduced without altering its gain — it depends on the ratio L/d independently of the individual dimensions d and L — so the plate thickness can

be shortened to ensure a small electron transit time. Using a Chevron stack with a proper geometry one can obtain pulses less than 1 ns wide, with rising times below 500 ps [18].

Over time, continuous electron collisions with the channel walls lead to an increase in the work function and thus a decrease in the gain. This means that MCPs have a fixed charge that they can amplify over their lifetime. Therefore, when multi-stage MCPs are used, the second and third ones often have a lifespan problem, as they are multiplying a greater number of electrons.

2.4.3 Detection efficiency

Although bare MCPs are directly sensitive to UV light, X-rays, ions, and electrons, the detection efficiencies are quite different. Due to the thickness of the channel walls most MCPs have an OAR of about 55% [19], which means that almost half of the input flux hits the metal plate instead of going into the channels. Additionally, the sensitivity of the detector strongly depends on the incident angle, energy, and kind of radiation. **Table 2.2** summarizes the efficiency of MCPs to several types of radiation.

Type of radiation		**Detection efficiency (%)**
Electrons	0.2 — 2 keV	50 — 85
	2 — 50 keV	10 — 60
Positive ions	0.5 — 2 keV	5 — 85
(H+, He+, Ar+)	2 — 50 keV	60 — 85
	50 — 200 keV	4 — 60
UV light	300 — 1100 Å	5 — 15
	1100 — 1500 Å	1 — 5
Soft X-rays	2 — 50 Å	5 — 15
Hard X-Rays	0.12 — 0.2 Å	∼1

Table 2.2: MCP detection efficiency. Taken from [18].

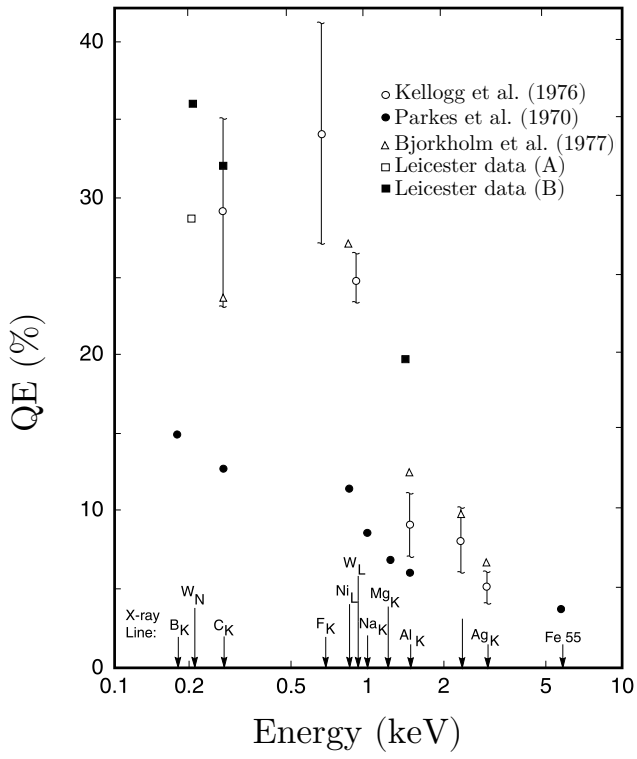

Figure 2.10: QE vs. Soft X-ray energy. Figure from [20].

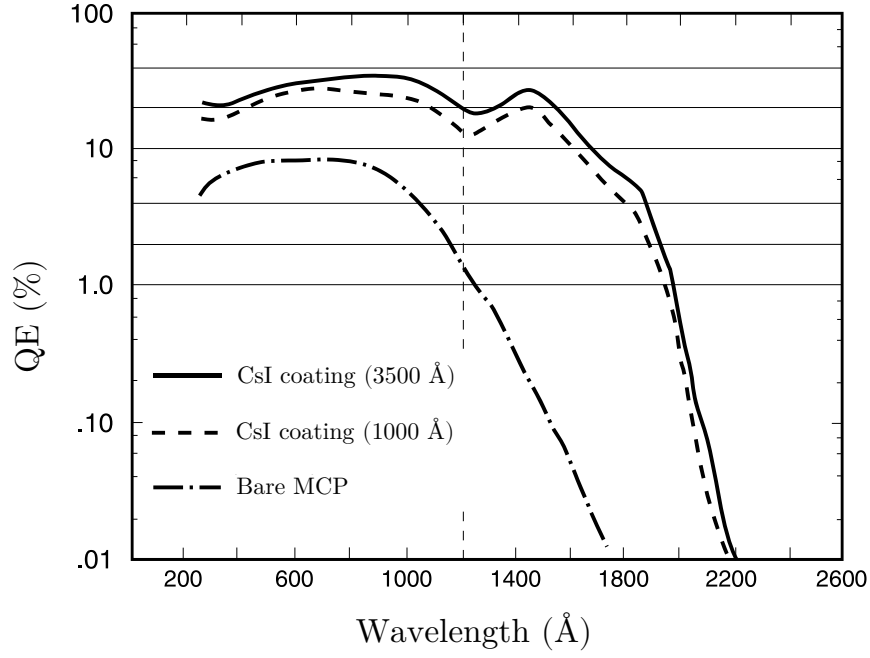

Figure 2.11: QE vs. UV wavelength for different thicknesses of CsI coatings. Figure from [21].

The detection efficiency for UV and X-rays — which is the range we are interested in — is relatively low compared to electrons and ions. When talking about photons, it is convenient to refer to Quantum Efficiency (QE), which is simply the ratio of incident photons to converted electrons. **Figure 2.10** shows the QE of bare MCPs in the soft x-ray region.

It has been proven that coating a photoelectric material (CsI, Au, MgF_2, etc.) on the MCP input surface enhances its QE [22]. As **Figure 2.11** illustrates, a CsI coating can improve the QE by a factor of 3 in the extreme UV region and by a factor of 1000 in the far UV range. Efficiency drops sharply to zero for the longer wavelengths as these photons do not have enough energy to rip off an electron.

A detailed theoretical model contrasted with experimental results can be found in [22, 20]. Reference [23] also offers a large collection of measurements on MCP quantum efficiency.

2.4.4 Imaging with a Delay Line Anode

As mentioned above, using specific anodes one can obtain position-sensitive readouts with an MCP. There is a wide variety of devices that allow for this: phosphor screens [24], pixelated anodes [25], resistive encoders [26], and so on. One of the most used, not only for its simplicity and low cost but for its compact assembly and high spatial resolution, is the Delay Line Anode (DLA).

A DLA consists of a long, coiled up wire placed after the MCP. The electron avalanche which leaves the detector hits the coil at a certain position, creating a signal that travels to both ends of the wire. The delay line detects the location of the incident event from the relative time difference of the arrival times of these signals. By using a second wire plane perpendicular to the first one, a two-dimensional image can be reconstructed. This is represented in **Figure 2.12**.

The impact position (X, Y) is given by the following equation:

$$X = \frac{1}{f_X}\left(t_{X1} - t_{X2}\right), \qquad Y = \frac{1}{f_Y}\left(t_{Y1} - t_{Y2}\right) \ ; \tag{2.12}$$

where $t_{X1},\ t_{X2},\ t_{Y1},\ t_{Y2}$ are the arrival times corresponding to each of the four signals and $f_X,\ f_Y$ are constants that depend on the geometry of the delay line.

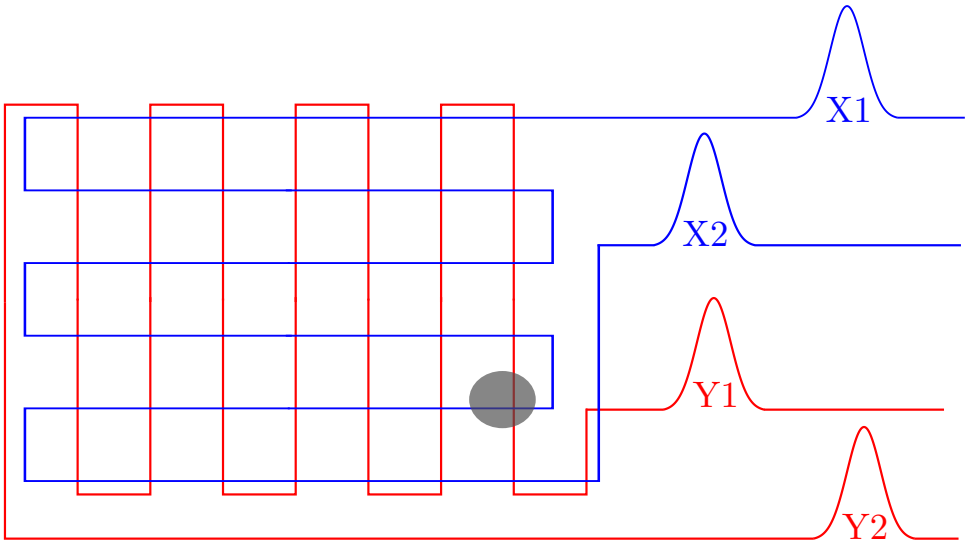

Figure 2.12: Working principle of the delay line. The position of the event is calculated from the time difference between X1 and X2, and Y1 and Y2.

2.5 Diffraction gratings

A diffraction grating is an optical device that splits light composed of different energies into its components. It may be viewed as a collection of slits separated by a distance comparable to the wavelength of the light, where each of these slits will act as a secondary source of diffracted light. The light diffracted by every groove interferes with each other and, as a result, it propagates into discrete directions.

In a reflection grating, the incident and the diffracted beams lie on the same side of the grating, while in a transmission grating they are on opposite sides. In both cases, only when the optical path difference between rays passing through adjacent grooves is a multiple of the wavelength, interference will be constructive. At all other angles, the beams will interfere destructively. As shown in **Figure 2.13**, in a transmission grating the path difference is $d\sin\alpha - d\sin\beta$. For a reflection grating, the same expression is valid but with a plus sign. Therefore, for a given groove distance d, the incident angle α and the diffraction angle β satisfy the following relationship:

$$d(\sin\alpha \pm \sin\beta) = m\lambda \ , \tag{2.13}$$

which is known as the grating equation. It is very common to express it in terms of the

groove density $N = 1/d$ or number of grooves per millimeter:

$$\sin\alpha \pm \sin\beta = Nm\lambda \ . \tag{2.14}$$

Here, m is the diffraction (or spectral) order and is always an integer.

For a polychromatic beam incident at a fixed α value, the different wavelengths are separated at different β angles. Indeed, from (2.13) one obtains:

$$\beta = \pm \arcsin\left(\frac{m\lambda}{d} - \sin\alpha\right) \ . \tag{2.15}$$

In the special case of $m = 0$, $\beta = \mp\,\alpha$ and the beam is reflected or transmitted without splitting up the wavelengths. It is evident from this equation that a grating produces an overlap between different diffraction orders, e.g. light of wavelength λ in the $m = 1$ order will be diffracted with the same angle as light of wavelength $\lambda/2$ with $m = 2$ and $\lambda/3$ with $m = 3$, etc (see **Figure 2.14**). This superposition is inherent to the grating and cannot be removed, so it must always be taken into account — especially when performing spectroscopic measurements. It is also worth mentioning that only the spectral orders which satisfy $|m\lambda/d| < 2$ exist; otherwise, the grating equation has no solution. For $\lambda/d << 1$, this is no longer a problem as a large number of diffraction orders exist and only the first ones are intense enough to be detected.

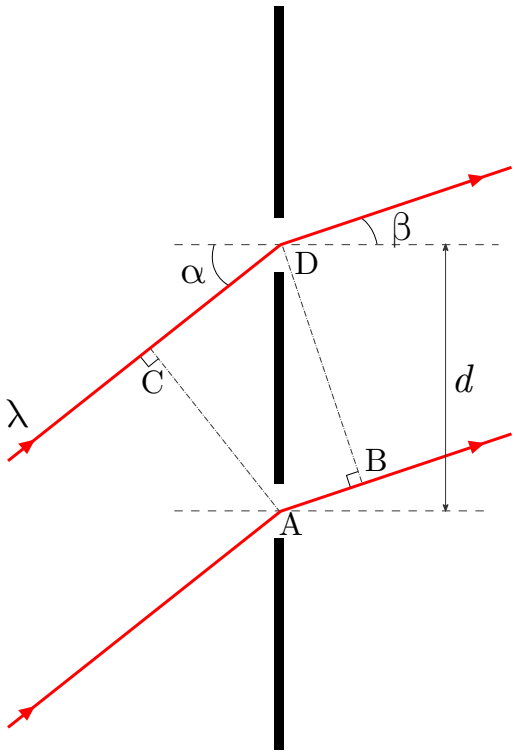

Figure 2.13: Schematic of a transmission grating. When the optical path difference $\overline{CD} - \overline{AB}$ equals a multiple of the wavelength, light from adjacent grooves interferes constructively.

Since the primary purpose of a grating is to split light by its wavelengths, it is important to know how the diffraction angle behaves when λ changes. Considering the angle of incidence as a constant, differentiating **Equation (2.14)** leads to

$$\frac{\mathrm{d}\beta}{\mathrm{d}\lambda} = \frac{Nm}{\cos\beta} \ . \tag{2.16}$$

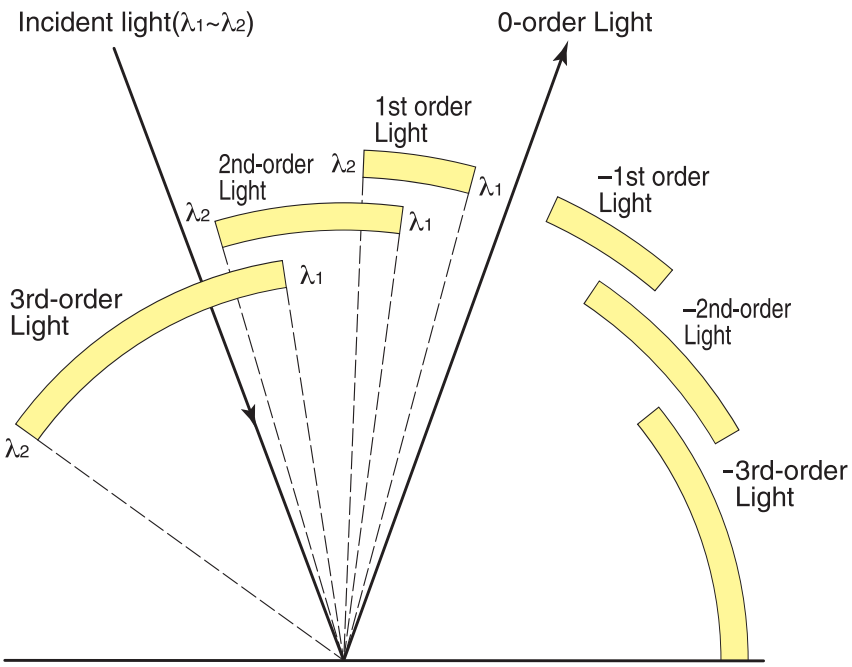

Figure 2.14: Diffraction orders and overlapping. Taken from [27].

This quantity is called angular dispersion. As β depends on m, it is more convenient to substitute the grating equation in the previous formula, which results in

$$\frac{\mathrm{d}\beta}{\mathrm{d}\lambda} = \frac{\sin\alpha \pm \sin\beta}{\lambda\cos\beta} \ . \tag{2.17}$$

This shows now that for a given wavelength, the angular dispersion depends only on the angles of incidence and diffraction. Inverting both sides of the equation and dividing by the focal distance of the system f yields

$$D = \frac{1}{f}\frac{\mathrm{d}\lambda}{\mathrm{d}\beta} = \frac{\mathrm{d}\lambda}{\mathrm{d}x} = \frac{\cos\beta}{Nmf} \ , \tag{2.18}$$

which is called the reciprocal linear dispersion and represents the change in wavelength corresponding to a change in location along the spectrum.

The resolving power R of a grating is a measure of its ability to separate neighboring spectral lines λ and $\lambda + \Delta\lambda$, and is given by the formula [28]:

$$R = \frac{\lambda}{\Delta\lambda} = mN \cdot W \ . \tag{2.19}$$

Here, W is the width of the grating, therefore $N \cdot W$ is the total number of grooves in the direction of the incident light. The reciprocal of R can be thought as the resolution, but note

that a diffraction grating is normally used together with other optical elements — e.g. when incorporated in a spectrometer. This means that, due to imperfections and aberrations in other elements, as well as the size of the slits, the actual minimum wavelength $\Delta\lambda$ that can be resolved will be larger and the resolution for the optical system will be lower than the one defined in **(2.19)**.

Chapter 3

Setup and tests

In this chapter, the development of a test setup for the spectrometer for SIS100 is described. We start with the assembly of the test setup, followed by the first measurements to characterize the detector, and ending with the acquisition of an x-ray spectrum. The whole process has been carried out at the *Institut für Kernphysik* in Münster.

3.1 Test setup in Münster

To achieve the energy-resolved detection, an MCP detector is combined with a position-sensitive delay line anode and a diffraction grating (see **Section 2.4** & **Section 2.5**). This section provides information about all the components used to build the spectrometer. Some technical drawings, with the distances and dimensions of the components, can be consulted in **Appendix A**.

3.1.1 Spectrometer

MCP detector & delay line

We used an MCP detector from the former WITCH experiment at ISOLDE which is already mounted inside a vacuum chamber. The setup includes two MCPs in a Chevron configuration placed on top of a delay line anode, as well as protection plates and electrical connections (**Figure 3.1**). The MCPs are from the *Long Life Series* of *Photonis* and both are coated with a thin emissive layer of SiO_2.

The delay line anode consists of two coils — one for the X direction and the other for the Y direction — and a "Holder". The "Holder" has a metal core and a ceramic, insulation

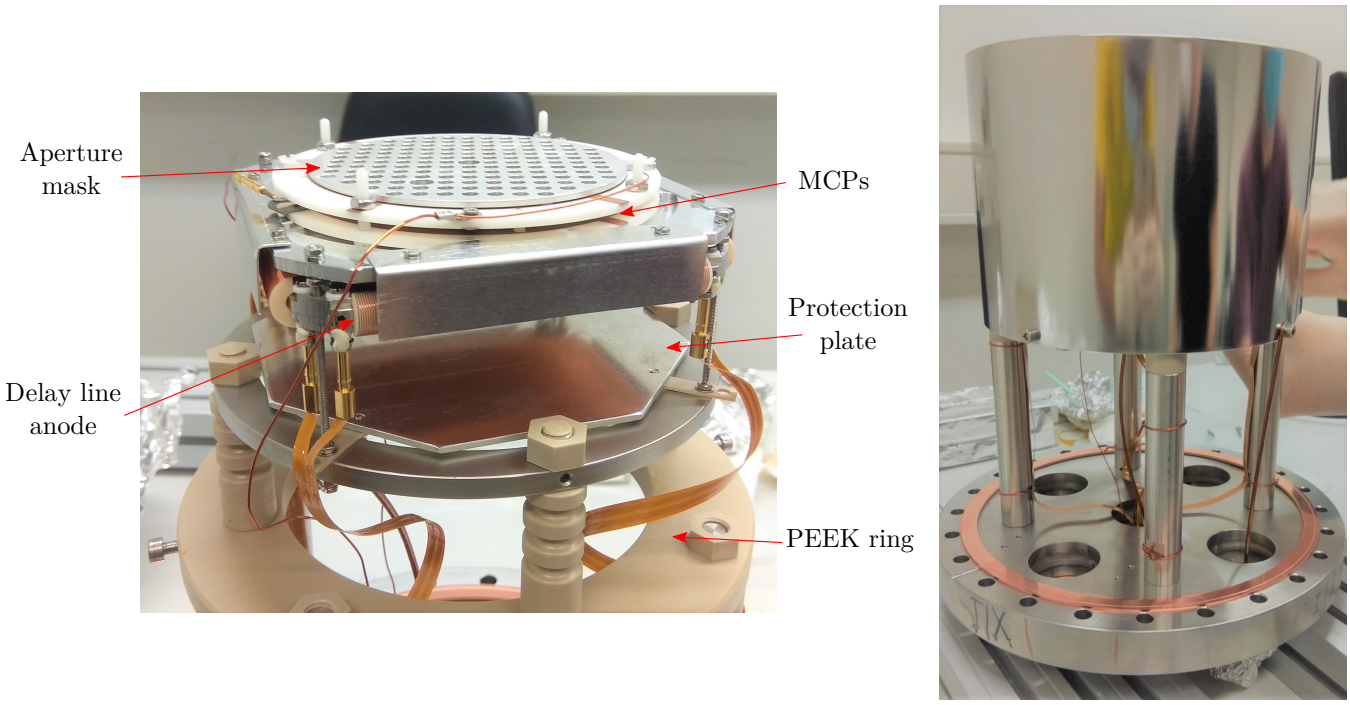

Figure 3.1: Pictures showing the MCP assembly. As seen on the second photo, everything is surrounded by a cylindrical electrode and placed on four mounting legs attached to a flange. The PEEK ring insulates the detector from the legs. The aperture mask was used to perform the position calibration (see **Section 3.2**).

holding structure, around which the coils are convoluted. Each coil has a "Reference" wire and a "Signal" wire. A potential difference of 20 V to 50 V is applied between "Signal" and "Reference", ensuring that the electron cloud that comes from the MCP is mostly collected on the "Signal" wires. For noise reduction, at the end of each coil the signal from "Reference" is subtracted from the corresponding signal of "Signal", being the four resulting pulses the outputs of the delay line anode (X1, X2, Y1, Y2). Peter Friedag's Ph. D. thesis [29] deals with the assembly of the detector and the delay line and should be consulted for all the technical information and specifications.

Diffraction grating

We ordered a *30-003 Laminar-type Replica Diffraction Grating* from *Shimadzu*. It is suitable for a wavelength range from 1 nm to 7 nm, corresponding to photon energies from approximately 1240 eV down to 177 eV. The optimal mounting parameters, provided by the manufacturer, are listed in **Table 3.1** and **Figure 3.2**.

The grating is placed on a holding structure (**Figure 3.3**) that can be moved and rotated by means of a vacuum manipulator (**Figure 3.4**). Its optimal position is studied in **Section 3.4**.

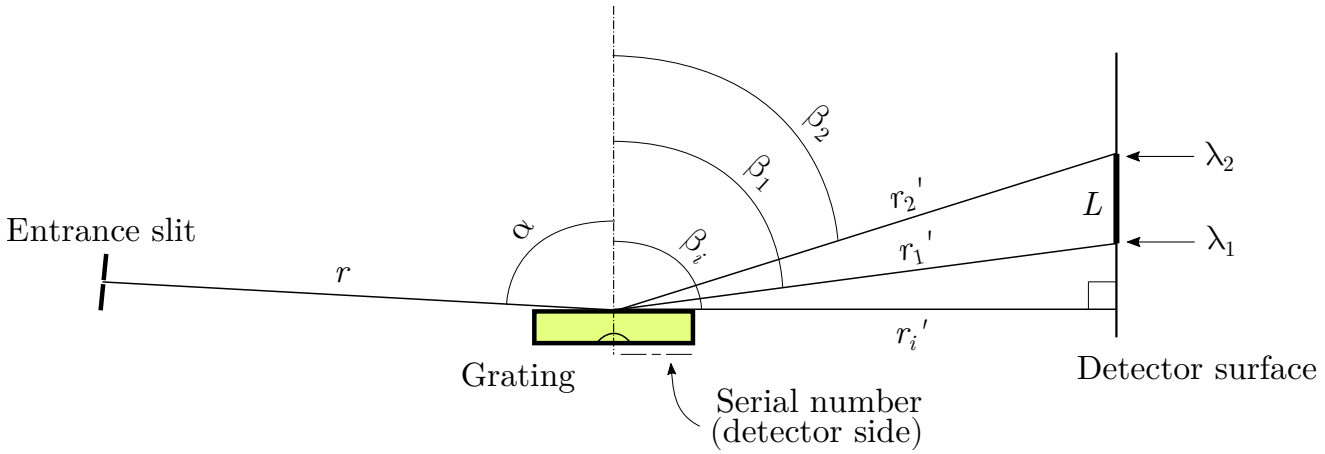

Figure 3.2: Mounting diagram of the grating.

Code number	**Groove density N (gr/mm)**	**Wavelength range λ_1–λ_2 (nm)**	**Image length L (mm)**	**Dimensions WxHxT (mm)**	**Coating material**
30-003	2400	1–7	26.8	50x30x10	Au

Mounting parameters

r (mm)	α (°)	r'_1 (mm)	β_1 (°)	r'_2 (mm)	β_2 (°)	r'_i (mm)	β_i(°)
236.7	88.60	235.8	85.79	239.5	79.39	235.0	90.53

Table 3.1: Grating specifications and mounting parameters.

X-ray source

To test the spectrometer, we are using a *642-1* x-ray source from *McPherson*. It is a de-mountable soft x-ray tube that includes a power supply, a cooling fan, an electron gun, and an interchangeable anode (**Figure 3.5**). The voltage can be set from 2.5 kV up to 10 kV in 0.1 kV increments, and the emission current can be adjusted between 0 and 1000 µA in 25 µA increments. The x-ray tube has no special shielding, but x-rays at these relatively low energies are absorbed inside the walls of a conventional vacuum chamber. The source comes with an Al anode and a Mg anode and, moreover, it provides an empty holder so that the user can install his own anodes.

The x-ray source should always be operated in a vacuum better than 10^{-5} mbar, otherwise, the filament of the electron gun will be damaged. In addition, the cooling fan must be on during the operation so that the anode does not overheat.

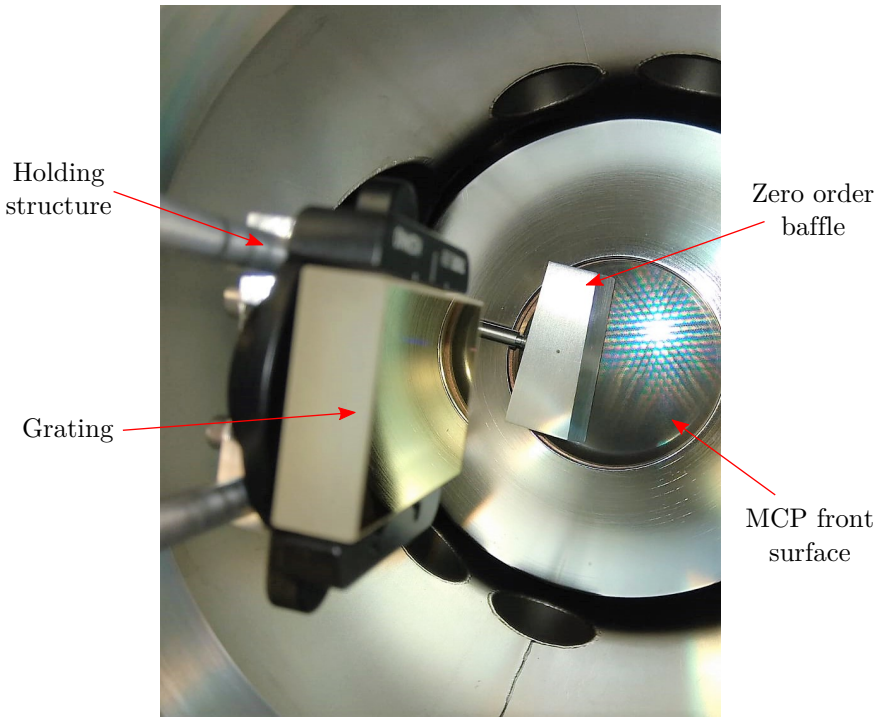

Figure 3.3: Photograph of the interior of the grating chamber.

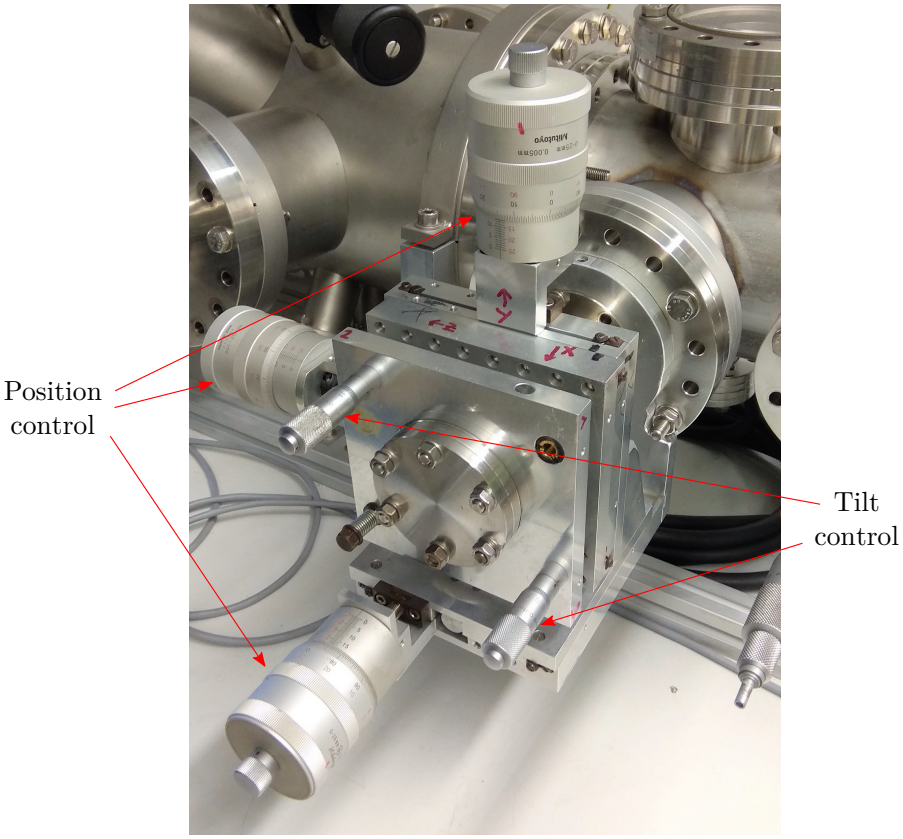

Figure 3.4: Vacuum manipulator used to control the position and rotation of the grating.

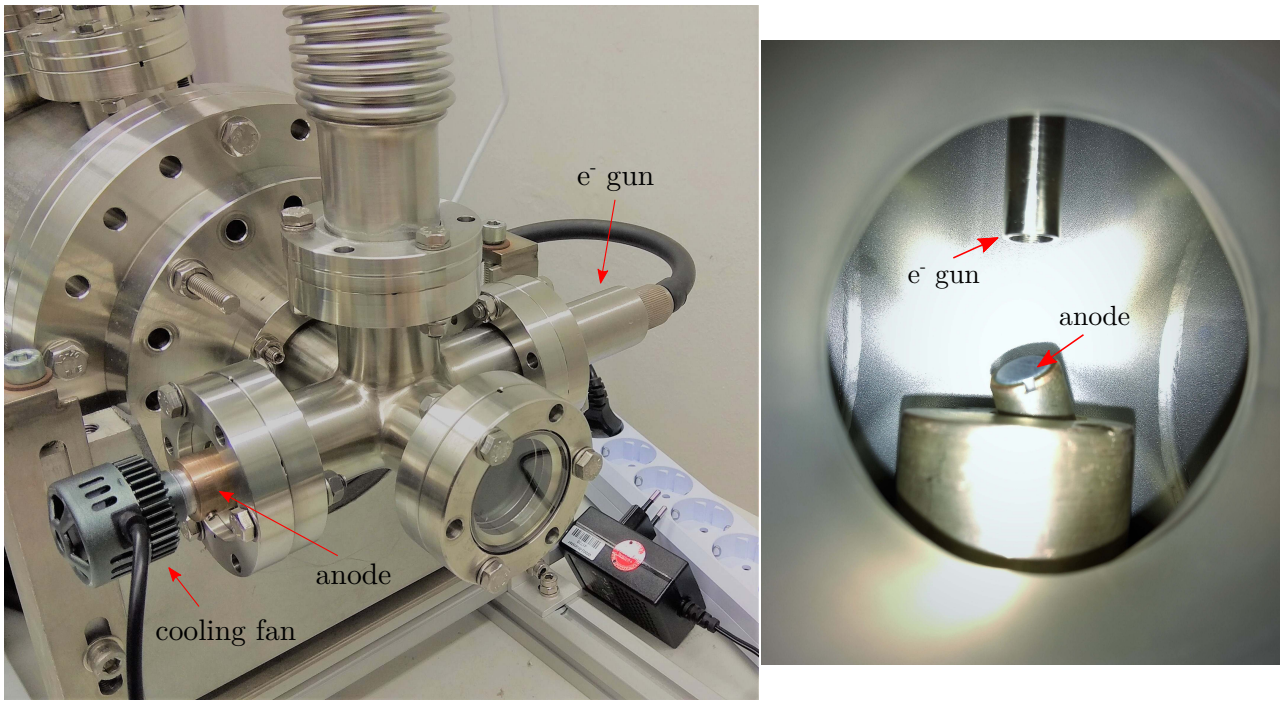

Figure 3.5: McPherson's 642-1 x-ray source. The second picture shows a top view from the inside.

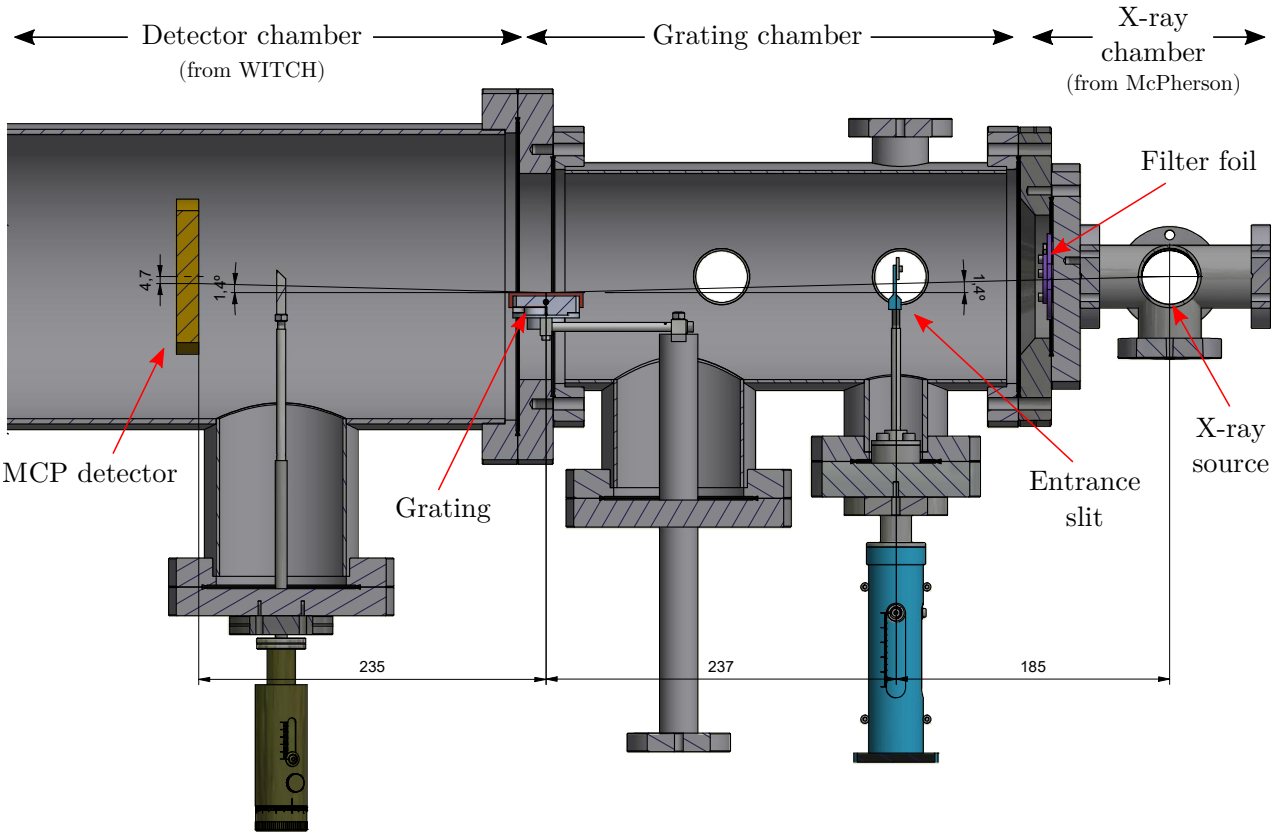

Figure 3.6: Simplified model showing the three vacuum chambers of our setup. Technical drawing by Christian Huhmann.

Vacuum chamber

Following the mounting parameters in **Table 3.1**, a custom vacuum chamber for the grating has been designed and built. **Figure 3.6** shows the first CAD model of the setup, including the MCP, a baffle, the grating, an entrance slit, a filter foil and the x-ray source. Note that the grating is located at the union between the existing detector chamber and the new grating chamber, making it difficult to insert the parts.

Two pumps are used to produce the vacuum inside the chambers: a *Pfeiffer MVP 040-2* (forepump) and a *Pfeiffer TC 400* (turbopump). The first one can pump from atmospheric pressure to a few millibars, while the second can achieve ultra-high vacuum (10^{-9} mbar). A pressure gauge (*IONIVAC ITR 90* from *Leybold*) is attached to the grating chamber to monitor the vacuum level.

Filter foils

During the first tests, it was found that the anode from the x-ray source glows during the operation, emitting a high flux of UV and visible light as background radiation. By using suitable filter foils, this radiation can be blocked while the x-rays still pass through. For instance, micrometer-thick aluminum foils can be utilized, as shown in **Figure 3.7**.

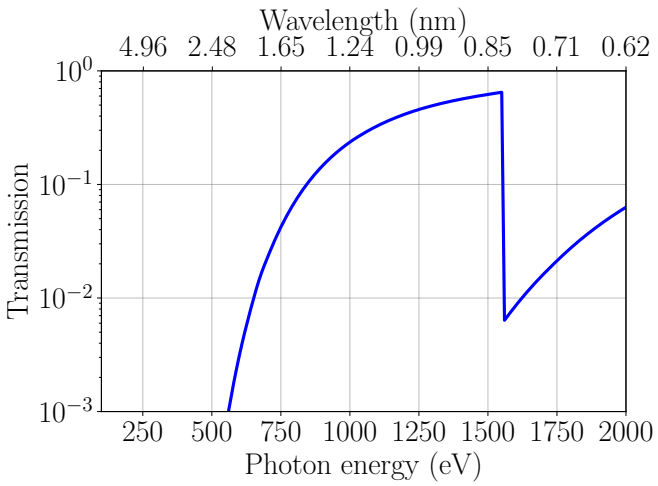

Figure 3.7: Transmission curve for a 4.5 µm thick aluminum foil. Data from [30].

We ordered two aluminum filter foils with different thicknesses from *Goodwell*: 0.8 µm and 4.5 µm. Two 0.8 µm sheets were combined to create a 1.6 µm thick aluminum foil. A special mounting frame was built to place the foil at the joint between the x-ray chamber and the grating chamber (**Figure 3.8**).

Ultrathin foil is among the most fragile material ever sold and will break if there is even the slightest pressure difference or vibration across it. Therefore, a very slow pumping mechanism must be designed so that the foil is unaffected by the air extraction from the chamber. If the foil acts as a window between two volumes — as in our case — this is particularly important and it will also be necessary to install a bypass between the two volumes. A typical small chamber pumping schedule would be 15 minutes for the first 10% of gas removal, 15 more minutes for the next 30%, another 15 minutes for the next 50%, and free pumping thereafter [31].

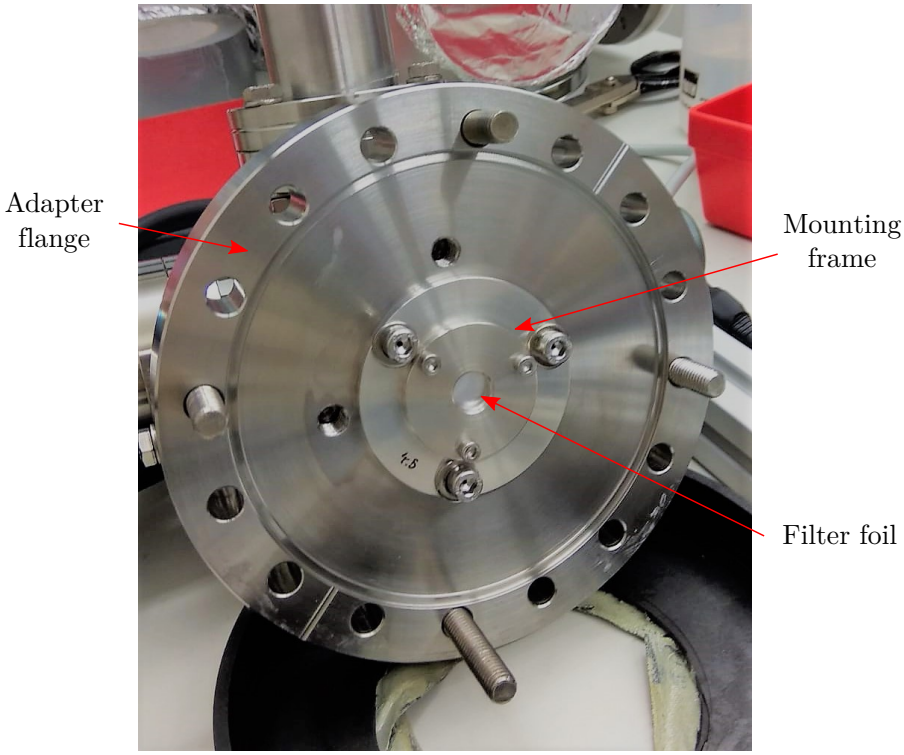

Figure 3.8: Mounting frame with the 4.5 µm Al filter foil.

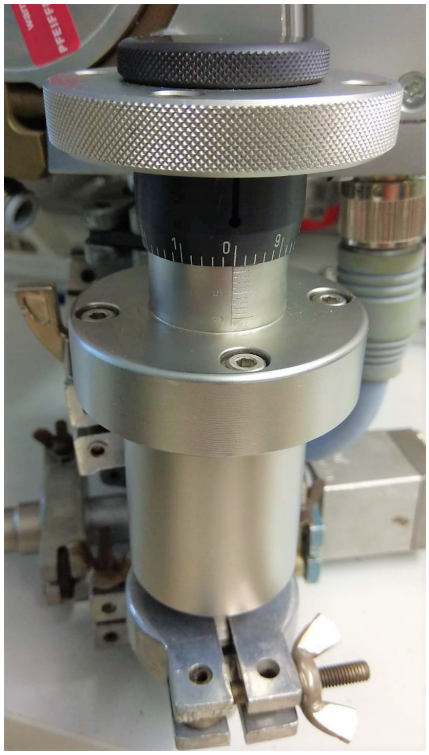

Figure 3.9: Needle valve.

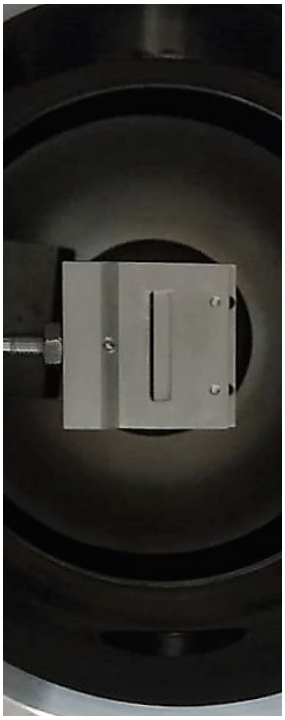

Figure 3.10: Entrance slit. The width can be adjusted by loosening the screws and moving the inner plate.

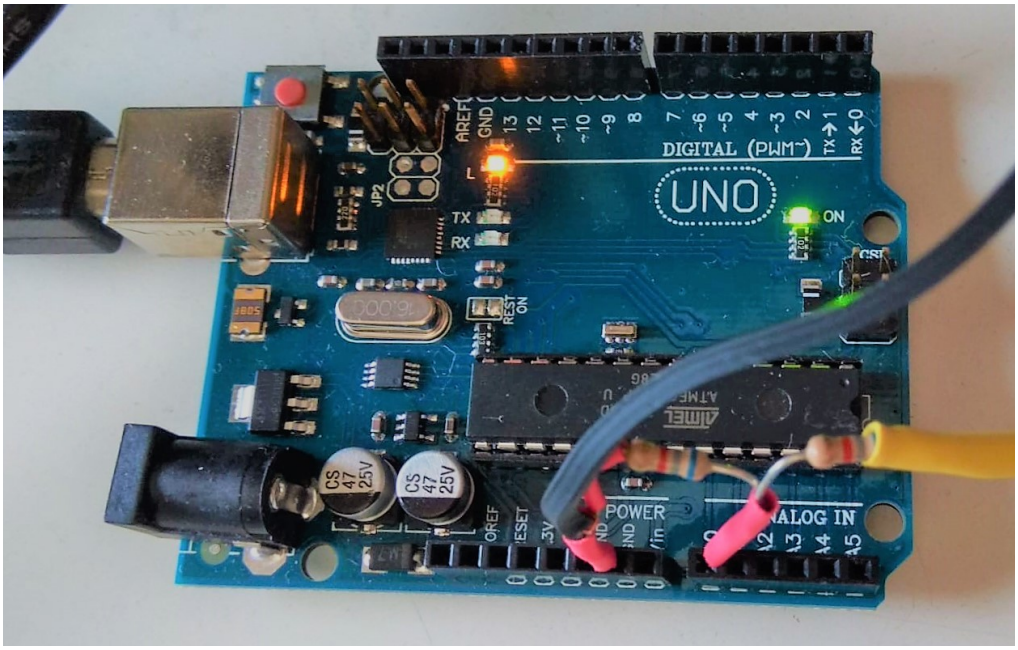

Figure 3.11: Arduino board used to monitor the vacuum inside the chamber. It gets an input voltage from the pressure gauge and passes the data to a computer.

We installed a bypass between the x-ray chamber and the detector chamber, as well as a needle valve that allows a very slow pumping and venting (**Figure 3.9**). This valve has a scale on it that goes from 0 to 10 mm and allows to control the pumping speed (10 mm corresponds to the largest opening). Before putting the filter in place, it was necessary to check that the process was slow enough. For this purpose, an Arduino board was connected to the pressure gauge to collect the data in real time (**Figure 3.11**). To prevent the filter from breaking, it was decided that the proper time to pump from atmospheric pressure to a few millibars should be about an hour and a half. After several tests, it was found that the valve should be in the 10 mm position when pumping and at 1.5 mm when venting, as shown in **Figure 3.12**.

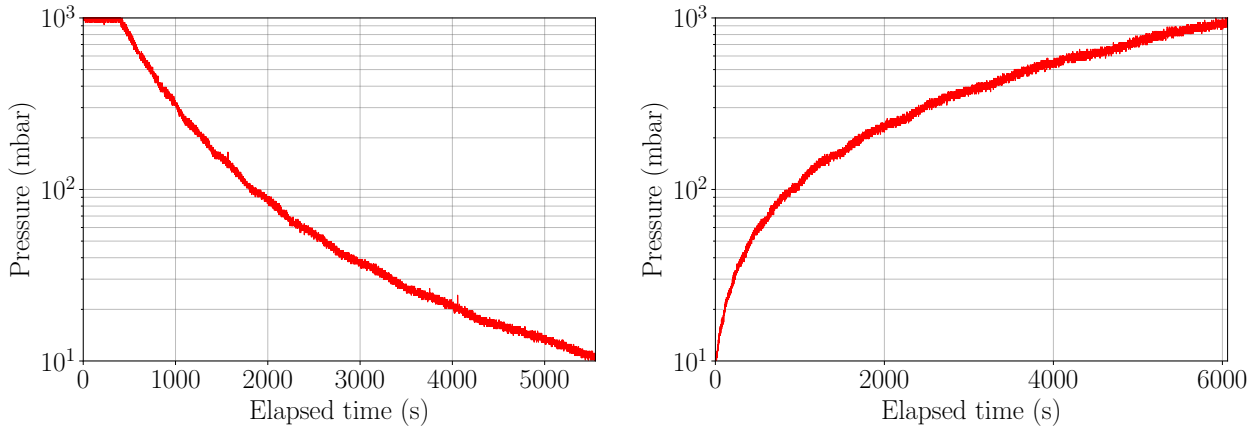

(a) Pumping test at 10 mm position. The elapsed time was 1h 32 min.

(b) Venting test at 1.5 mm position. The elapsed time was 1h 41 min.

Figure 3.12: Evolution of the pressure when pumping or venting through the needle valve.

Slit & zero-order baffle

In order to have a well-focused beam, an entrance slit of adjustable width was built and placed in the grating chamber (**Figure 3.10**). A rectangular piece made of aluminum was also built to block the zero-order light coming from the grating (direct beam reflection). The zero-order baffle is placed in front of the MCP stack, as can be seen in **Figure 3.3**. Both components are inserted into the vacuum chambers via linear feedthroughs. **Figure 3.18** shows a photo of the complete setup.

3.1.2 Electronics

The detector outputs five electric signals, one coming directly from the MCP and the other four from the delay line anode. After some signal processing, they are sent to a time-to-digital converter (TDC), which records the arrival times of the delay line pulses relative to the MCP pulse and sends the data to a computer. Here, the impact position on the detector is reconstructed using **Equation (2.12)**. **Figure 3.13** shows the diagram of the electronic chain used to process the signals and **Figure 3.17** shows the corresponding modules.

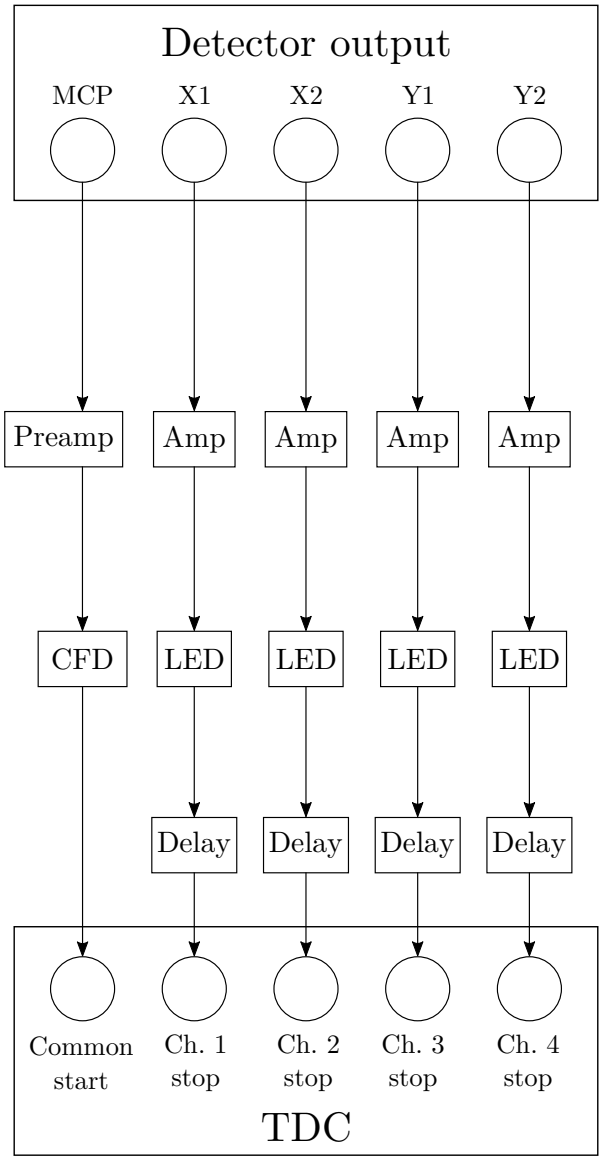

Figure 3.13: Signal processing diagram.

Power supply

The *NHQ 224M* power supply from *iseg* provides the high voltage for the MCP and the delay line. The different components — MCP front and back, holder, reference, and signal — require different voltages. The potential differences between the parts must be within the following ranges [29]:

- Front - back: from −2100 V to −2600 V.
- Back - holder: from 0 V to −250 V.
- Back - reference: from −550 V to −300 V.
- Reference - signal: from −20 V to −50 V.

This is managed by a voltage divider, that is encapsulated inside a box. The internal connections are shown in **Figure 3.14**. The voltage offset between Reference and Signal must be especially stable so it is applied by a battery box, the *Roent-Dek BA3*. It consists of three standard 12 V cells that provide a potential difference of 35 V – 40 V, depending on the load. Both devices are shown in **Figure 3.16**.

The high voltage must be set very slowly, particularly if the MCPs have been exposed to atmospheric pressure for a long time. Besides, the current should be monitored for possible

deviations from its expected value (indicating a problem). The power supply has a KILL switch that shuts it off when a certain voltage or current value is exceeded, these can be set with rotatory switches. It was found that the pressure gauge must be turned off when applying the voltage, because it creates many background signals that increase the current, thus triggering the KILL switch.

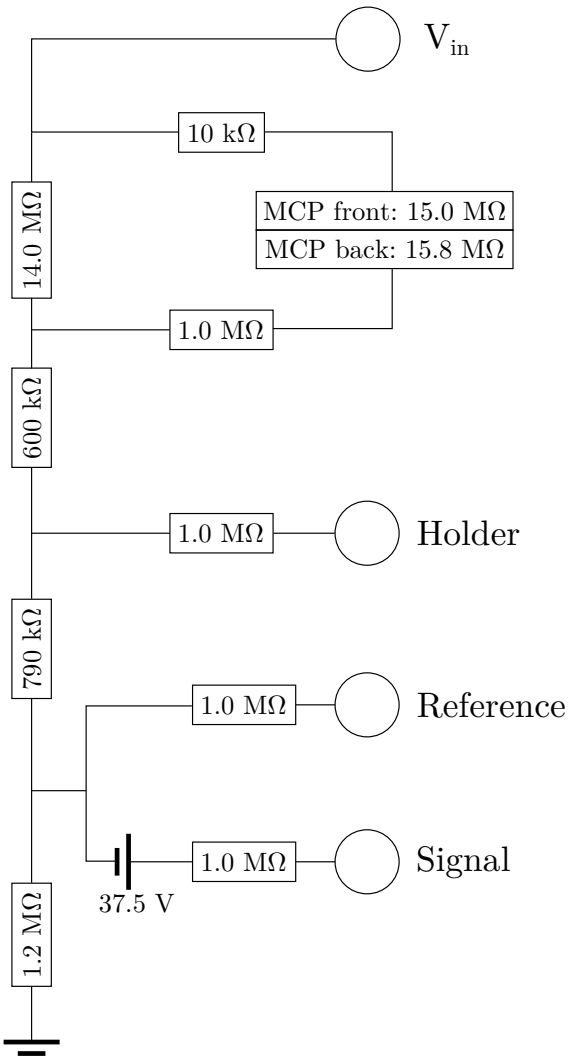

Figure 3.14: Schematic of the voltage divider. Protection resistances of 1 MΩ are inserted before each connection. From [29].

Amplifiers

The MCP back signal is amplified with the *RoentDek FAMP1+*, which has a nominal gain of about 55 and can be adjusted with a potentiometer from 0% to 110%. The delay line signals (X1, X2, Y1, Y2) are sent to the *CAEN N979* fast amplifier, where they are amplified by a factor of 10.

Discriminators

After amplification, the delay line signals are sent to the *CAEN N840* Leading Edge Discriminator (LED) that will reject pulses below a certain threshold (noise) and create NIM logical signals as output. Both the threshold and the output pulse width can be adjusted individually for each channel by means of a switch and a display.

The MCP signal goes to a Constant Fraction Discriminator (CFD), the *RoentDek CFD1x*. A CFD creates two signals when the incoming pulse is above a certain threshold, one is delayed while the other is attenuated and inverted. The ratio between both pulse heights f can be adjusted via a potentiometer on the front panel and the delay is set by an external coaxial cable. Then the signals are added and a trigger is given at the time of the zero crossing. It can be shown that this zero crossing appears always independently of the incoming pulse amplitude. **Figure 3.15a** illustrates this process and **Figure 3.15b** shows a comparison between leading edge and constant fraction triggering. Besides that, we often used the *CAEN N1145* counter to control the count rate of the MCP raw signal.

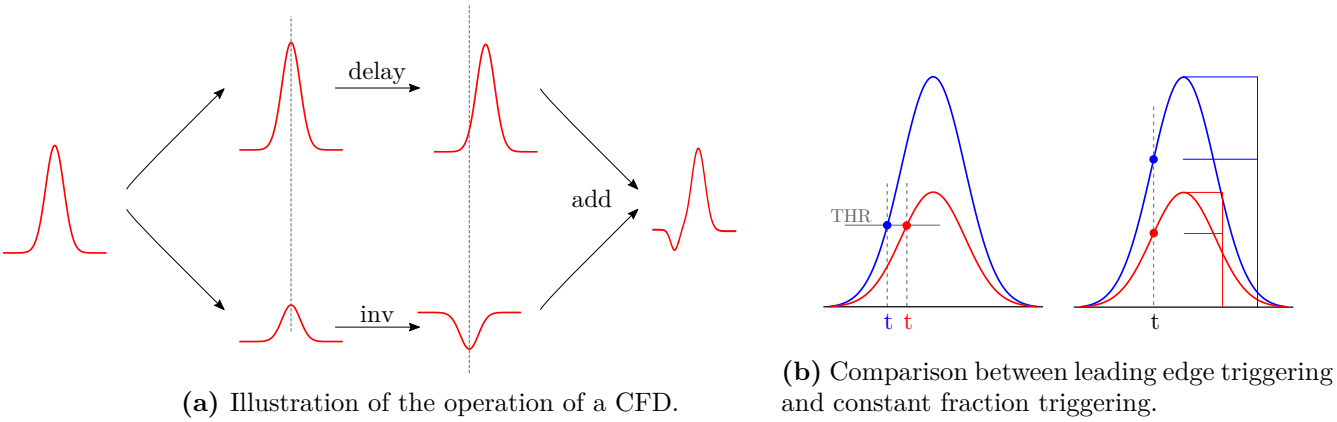

(a) Illustration of the operation of a CFD.

(b) Comparison between leading edge triggering and constant fraction triggering.

Figure 3.15: A simple threshold triggering causes a dependence of the trigger time on the pulse height, while a CFD triggers on a constant fraction of the total peak height, hence removing this dependency.

Time-to-digital converter

The MCP back signal is then used as the common start for the *CAEN V775N* time-to-digital converter. After introducing some delay with the *ORTEC GG8000* gate generator, the delay line pulses are used as stop signals for the first four TDC channels. A TDC converts the time difference between the start signal and the stop signal into a digital value, this way we obtain the arrival times of each delay line signal: t_{X1}, t_{X2}, t_{Y1}, t_{Y2}. The data acquisition is done through *FPPGUI*, a PC program written by Fred Zwarts (KVI Groningen) and Volker Hannen. It allows us to record the TDC data as well as to do online analysis and save the data in different formats.

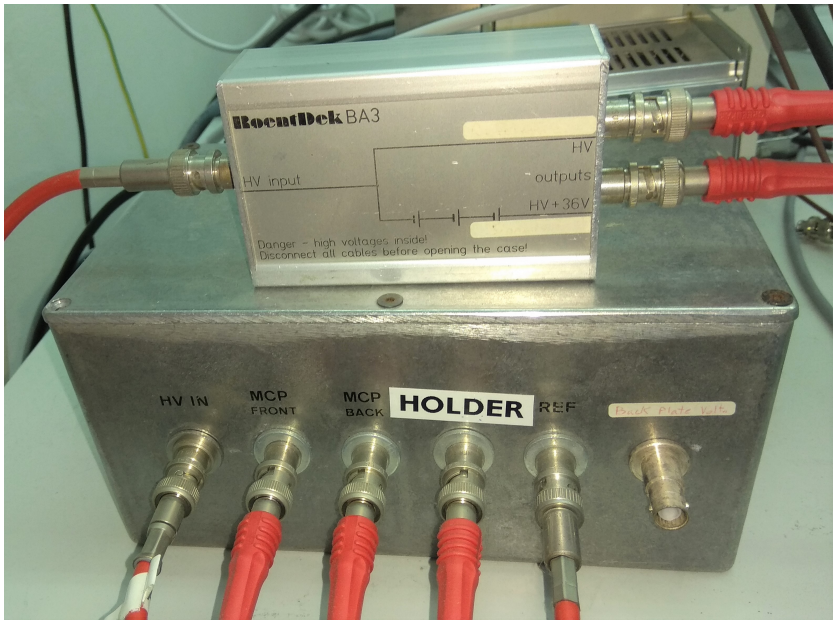

Figure 3.16: Picture of the voltage divider box and the battery pack *RoentDek BA3*.

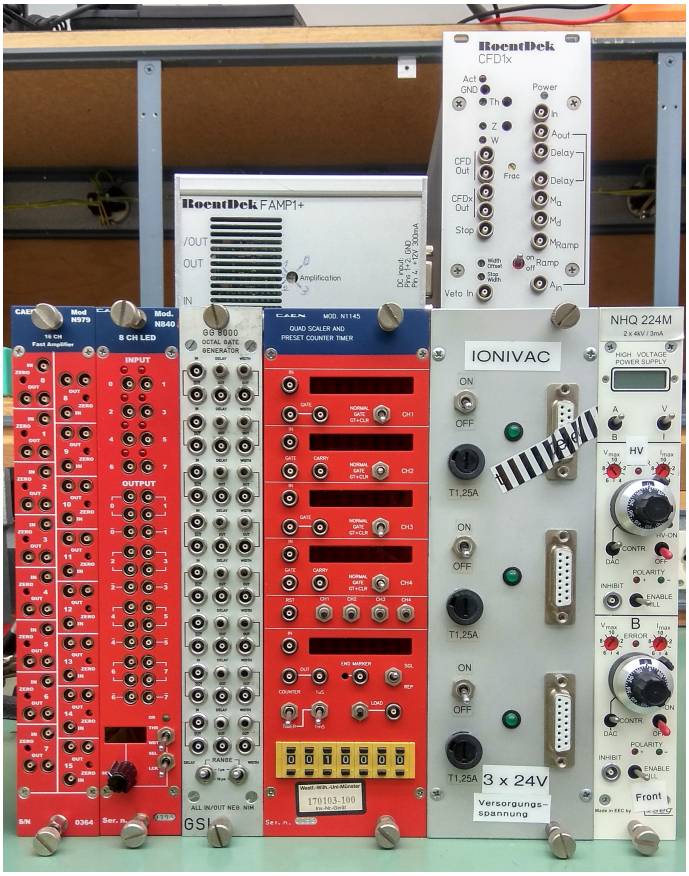

Figure 3.17: Electronic modules of the setup. From left to right: the *N979* Fast Amplifier and the *N840* LED from *CAEN*, the *GG8000* Octal Gate Generator, the *CAEN N1145* Counter, the pressure gauge power supply, and the *NHQ 224M* power supply. On top of them are the *RoentDek FAMP1+* and *CFD1x*.

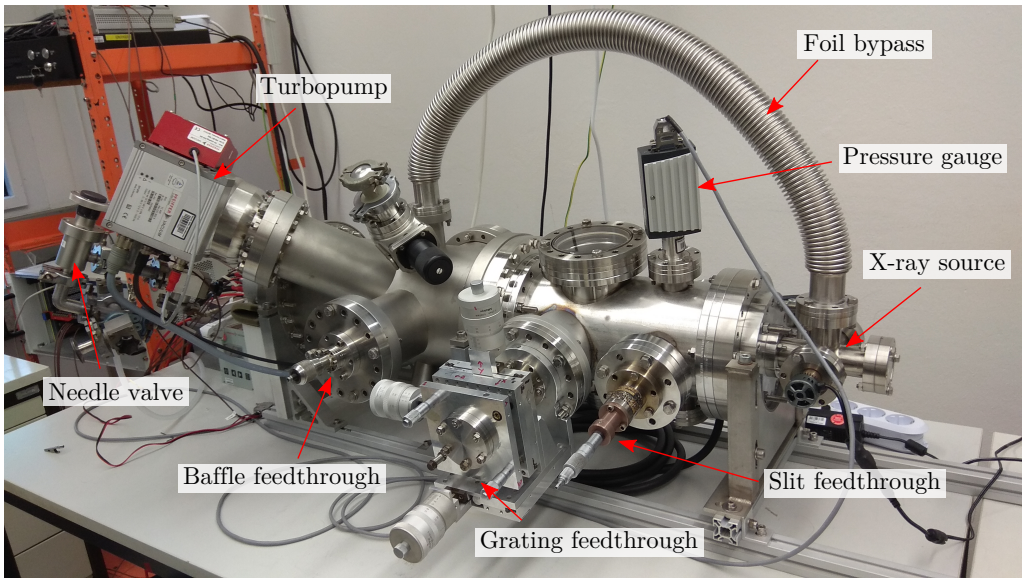

Figure 3.18: Picture of the full setup.

3.2 Position tests

The first tests were performed before installing the diffraction grating, the slit, and the baffle in order to check the position sensitivity of the detector. For that purpose, an aperture mask was screwed on top of the MCP stack, as can be seen in **Figure 3.1**. It consists of a 0.5 mm thick aluminum sheet with 4 mm diameter holes on it and a center-to-center spacing of 6 mm. The hole in the center and one in the upper right corner are bigger (6 mm diameter) to break the symmetry. The technical drawing can be found in **Appendix A**.

Since a single photon detection should be followed by four delay line signals, the thresholds of the CFD and LED were adjusted so that each MCP event triggers the first four channels of the TDC. This can be seen in **Figure 3.19**. It is also worth mentioning that the sum of

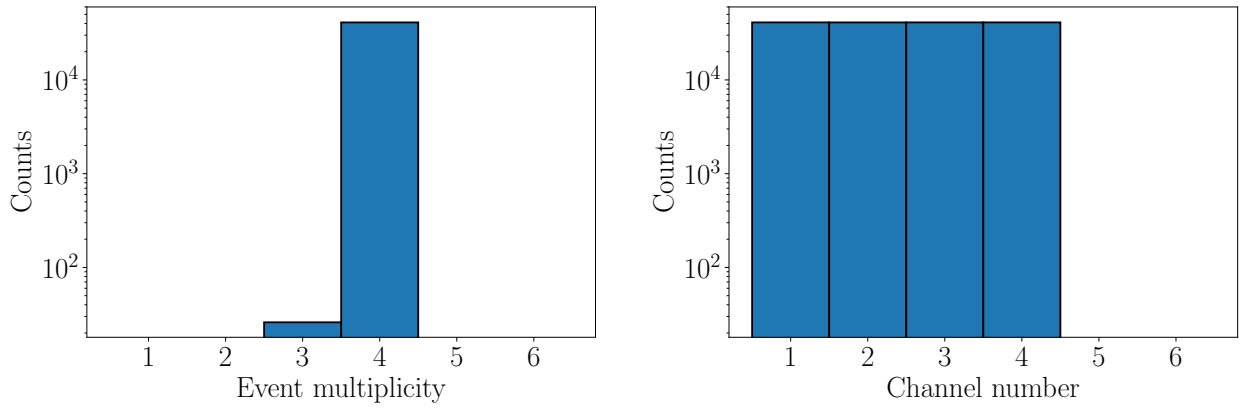

Figure 3.19: Event multiplicity and TDC channel triggerings after the threshold adjustment. As one detected photon creates four delay line pulses, the right graph must always be balanced and the left one should mostly include events of multiplicity four.

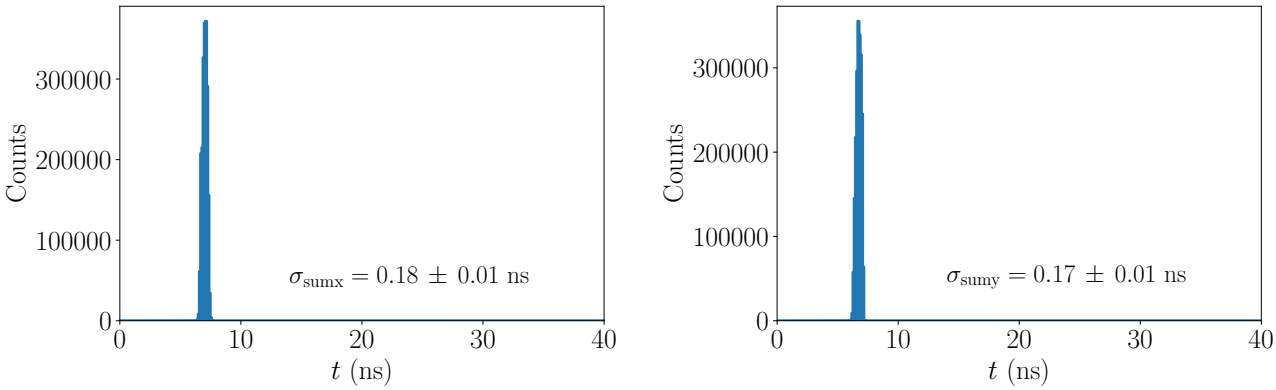

(a) $t_{X1} + t_{X2}$. **(b)** $t_{Y1} + t_{Y2}$.

Figure 3.20: Sum of the arrival times in each dimension. This quantity remains constant as it corresponds to the time it takes for a signal to travel from one end of the delay line to the other.

the arrival times in each dimension, i.e. $t_{X1} + t_{X2}$ and $t_{Y1} + t_{Y2}$, must remain constant since they are related to the total length of the delay line wires. This is shown in **Figure 3.20**. With *FPPGUI* one can do an online analysis and look at these graphs in real time, so it is always good to check that these conditions are met before starting a measurement.

After these checks, two position tests were done: one using a 260 nm UV diode and one using the x-ray source with the Al anode ($V = 2.5$ kV, $I = 100$ µA). The images produced by the detector are shown in **Figure 3.21**. The holes are well resolved and the two larger holes are distinguishable from the others. The figure also shows that the *Photonis* channel plates used are sensitive in the UV as well as the soft x-ray region. The QE in the x-ray region can unfortunately not be calculated from the measurements, as the x-ray source intensity is not calibrated. Several things to note about these images: the filter foil was installed for the x-ray measurement, acting as a smaller window and hence limiting the image formation. Besides that, the anode is not centered inside the chamber of the x-ray source (see **Figure 3.5**), which causes the image not to be completely symmetrical and to have more intensity on the right side.

The x and y positions were calculated from the difference between the arrival time of the delay line signals, i.e. $(t_{X1} - t_{X2},\ t_{Y1} - t_{Y2})$. However, by looking at **Equation (2.12)** one can see that it is also necessary to multiply by the constants $f_X,\ f_Y$ which are unknown. This is why the positions are initially in time units. Since we know that the center-to-center spacing of the aperture mask is 6 mm, a calibration can be done to find these values and transform

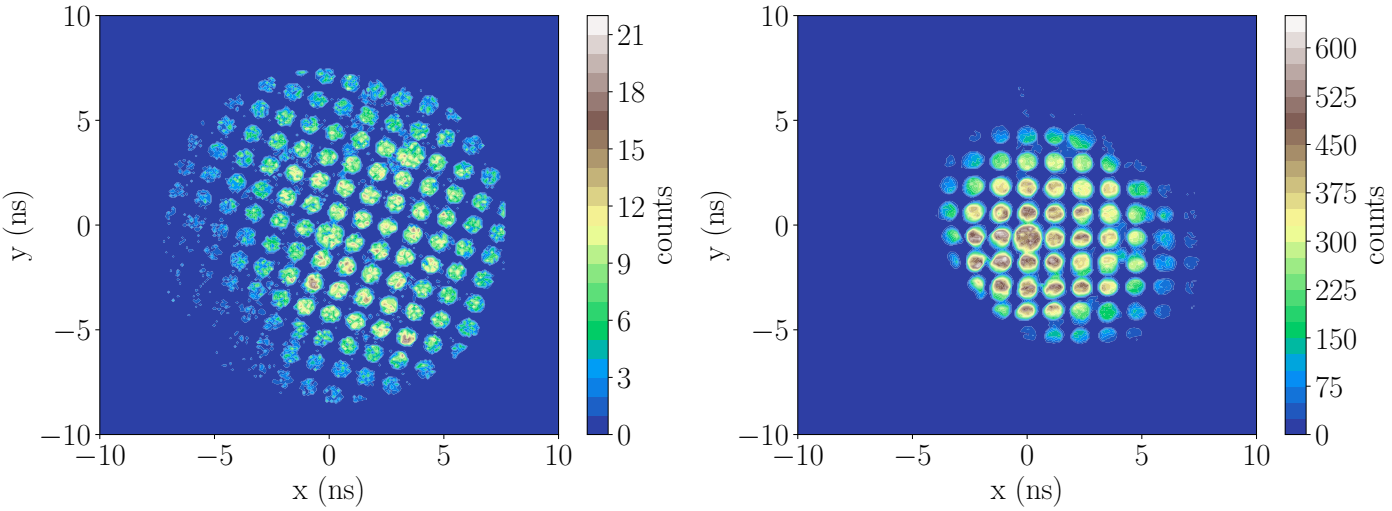

(a) LED measurement.

(b) X-ray measurement.

Figure 3.21: Images produced with the aperture mask and the UV and x-ray sources. In order to perform the position calibration, the second image was rotated by 16.75° (anticlockwise) so that the mask axes are aligned with the x and y axes.

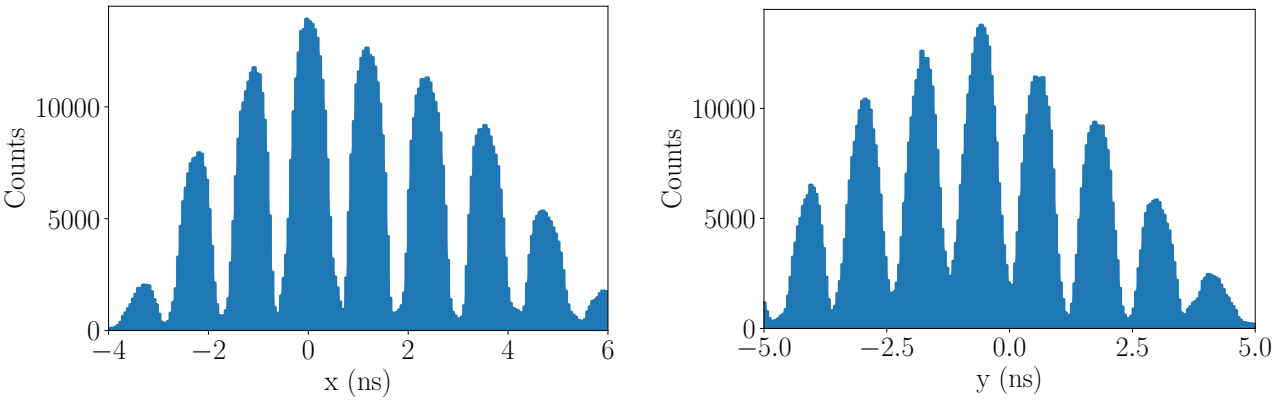

(a) Projection on the x axis, y $\in [-5, 5]$ ns.

(b) Projection on the y axis, x $\in [-4, 6]$ ns.

Figure 3.22: Projection of **Figure 3.21b** along the x and y directions.

the axes to millimeters. It was done as follows: first, the 2D histogram in **Figure 3.21b** was projected along the x and y dimensions (see **Figure 3.22**), then the mean distance between the peaks was calculated. Finally, by a simple rule of three, the conversion factors f_X, f_Y are found. The mean distance between peaks is $d_X = 1.167 \pm 0.001$ ns for the x-projection and $d_Y = 1.184 \pm 0.002$ ns for the y-projection. This leads to $f_X = 0.1945 \pm 0.0002$ ns mm^{-1} and $f_Y = 0.1974 \pm 0.0003$ ns mm^{-1}. The small difference in the conversion factors is caused by slightly different delays in the analog processing electronics.

3.3 Timing tests

The next tests were focused on the time response of the detector. After the amplification, the MCP signal was connected to an oscilloscope in order to determine its rise time and width. For more accuracy, 5050 waveforms were saved on a computer for later analysis. **Figure 3.23** shows one of these. Both the FWHM and the rise time — the time it takes for the leading edge of the pulse to rise from the 10% of its maximum height to the 90% — were calculated for each trace, and then the average values were computed. As a result, we obtained a rise time of $t_r = 6.449 \pm 0.013$ ns and FWHM $= 17.28 \pm 0.08$ ns.

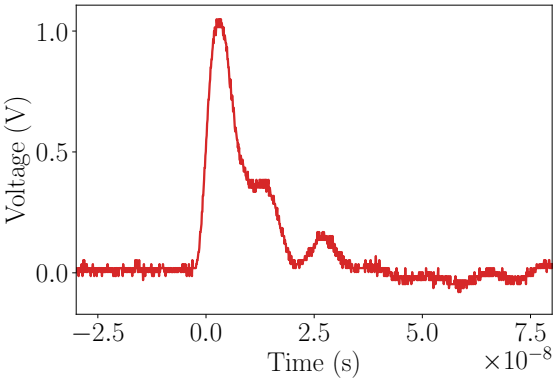

Figure 3.23: MCP output signal after amplification.

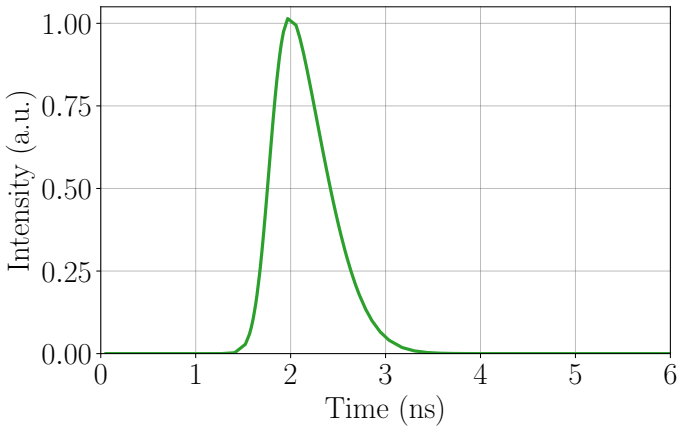

Figure 3.24: Pulse shape of the LED from *PicoQuant*. The datasheet specifies a FWHM of 664 ps.

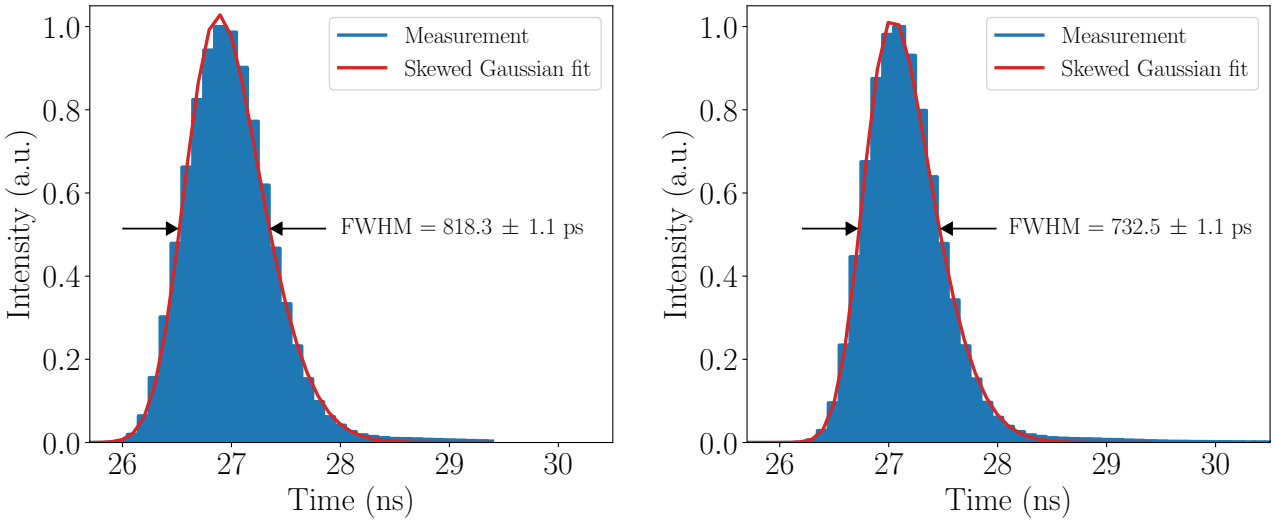

(a) High amplification.

(b) Low amplification.

Figure 3.25: Arrival time distribution of the MCP signal. A lower amplification seems to narrow the distribution.

In order to obtain the time resolution of our MCP detector, a 256 nm pulsed UV LED from *PicoQuant* was used as photon source. The pulse shape is provided by the manufacturer (**Figure 3.24**). The LED pulses were triggered by a function generator and the trigger signals were also used for the common start of the TDC. The MCP back signal was recorded on the TDC channel 5. In this way, we get an arrival time distribution of the MCP signals, and its width gives us an idea of the combined time resolution of the setup (MCP + LED + electronics).

Two measurements were performed: the first with a high amplification, the second with a lower one. The amplification factors are not very clear since they are manually adjusted by turning a screw, but for the first measurement it is close to the maximum (110%) and for the second one it was about half (50%). The results, along with a fit, are shown in **Figure 3.25**. Since these distributions result from the convolution of the LED pulse with the spectrometer response, they are not purely Gaussians but have a small tail on the right side, just as the LED pulse. The function that best fits the data is a skewed Gaussian.

After the fit, the FWHMs of both distributions were calculated, giving 818.3 ± 1.1 ps for the first measurement and 732.5 ± 1.1 ps for the second. It seems that using a lower amplification on the MCP signal improves the time resolution of the setup. As we want to know the time resolution of the detector, the LED contribution has to be removed from these

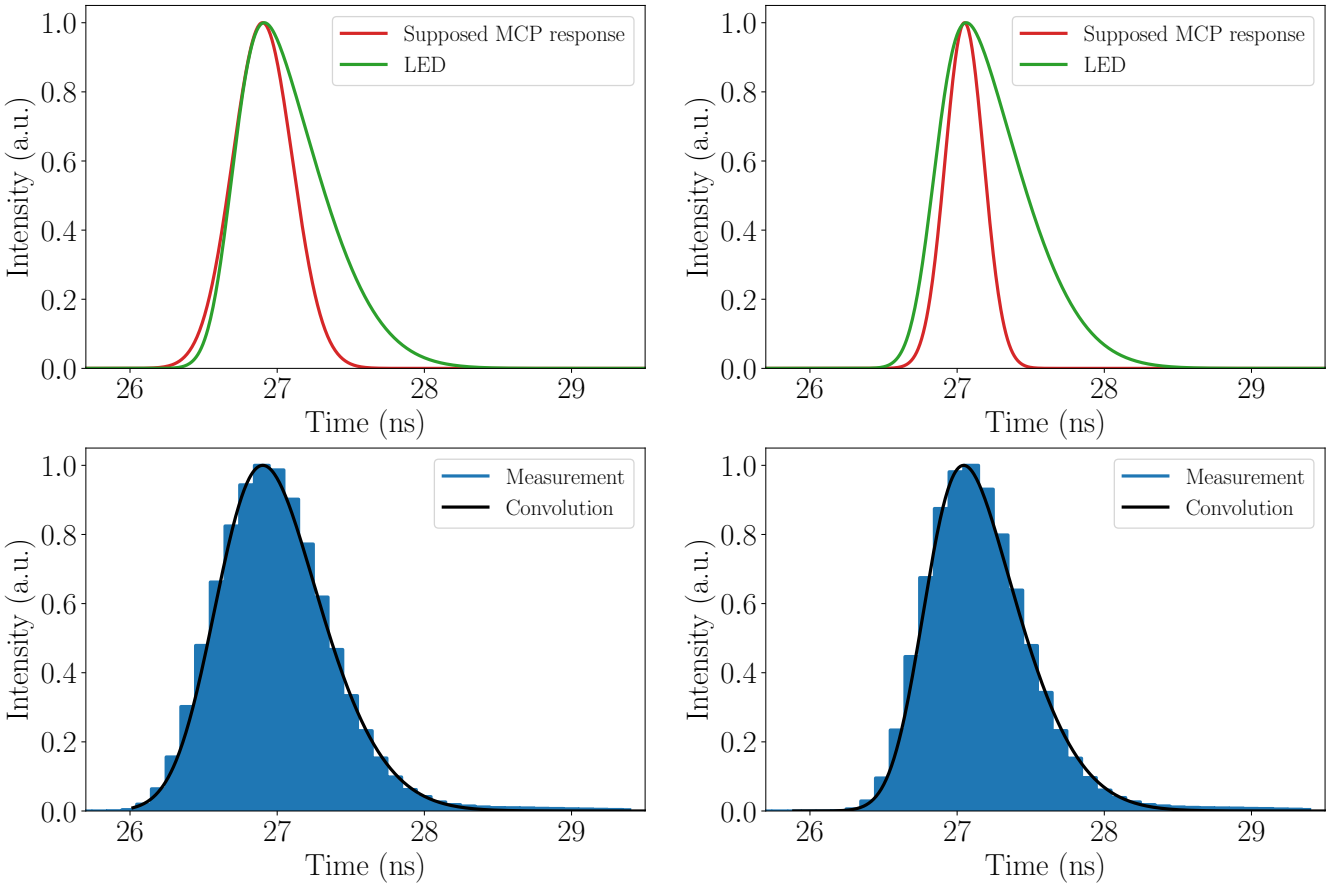

(a) High amplification.

(b) Low amplification.

Figure 3.26: The upper graphs show the assumed gaussian time distribution of the MCP signals together with the given shape of the LED pulses. The lower graphs display the measured distributions together with the convolution of the corresponding LED and MCP curves, showing the validity of our approximation.

values. We know that in a gaussian convolution the total width is the square root of the sum of the squared widths, in our case this means that:

$$\mathrm{FWHM}_{\mathrm{measured}} = \sqrt{\mathrm{FWHM}_{\mathrm{LED}}^2 + \mathrm{FWHM}_{\mathrm{detector}}^2} \ , \tag{3.1}$$

so the width of the detector (plus electronics) contribution is

$$\mathrm{FWHM}_{\mathrm{detector}} = \sqrt{\mathrm{FWHM}_{\mathrm{measured}}^2 - \mathrm{FWHM}_{\mathrm{LED}}^2} \ . \tag{3.2}$$

From the datasheet, we already know that the FWHM of the LED pulse is 664 ps. This finally leads to $\mathrm{FWHM}_{\mathrm{detector}} = 478.3 \pm 1.2$ ps for the high amplification measurement and $\mathrm{FWHM}_{\mathrm{detector}} = 309.2 \pm 2.7$ ps for the low amplification one.

We supposed that the time response of our setup follows a gaussian distribution with that FWHM — although it is important to note that it depends on the amplification of the MCP signal. To crosscheck, we can convolute the supposed gaussians with the LED pulse and the results should look similar to the original measurement. As can be seen in **Figure 3.26** the results match perfectly, showing that our assumption is correct.

3.4 Setup optimization

After the position and timing tests, the aperture mask was removed and the filter foil, the slit, the diffraction grating, and the zero-order baffle were installed. This concludes the building of the spectrometer test setup (**Figure 3.18**), which is now able to acquire spectra. **Figure 3.27** shows some images produced (without the baffle) by this setup. Here, the magnesium anode was used and the x-ray source was set to a voltage of 2.5 kV and an intensity of 100 µA. The slit opening was adjusted to 0.3 mm and the voltage supplied to the MCP was 3 kV. The x-rays pass through the filter and slit, and a vertical beam is formed. Then the beam reaches the grating, and the photons hitting at the correct angle (grazing angle of 1.4°) are diffracted according to **Equation (2.13)**. The incident beam and the zero-order reflected light can be seen in **Figure 3.27a** — note that the grating is covering part of the beam and therefore its shadow is visible. The first-order light is barely noticeable due to its low intensity compared to the others. When inserting the zero-order baffle, the direct beam and the zero-order line are blocked, making it possible to see the higher-order lines, as in **Figure 3.27b**.

Now that the complete setup is ready, the next step is to place the grating and the slit in their optimal positions, so that the spectrometer has the best possible resolution. To achieve

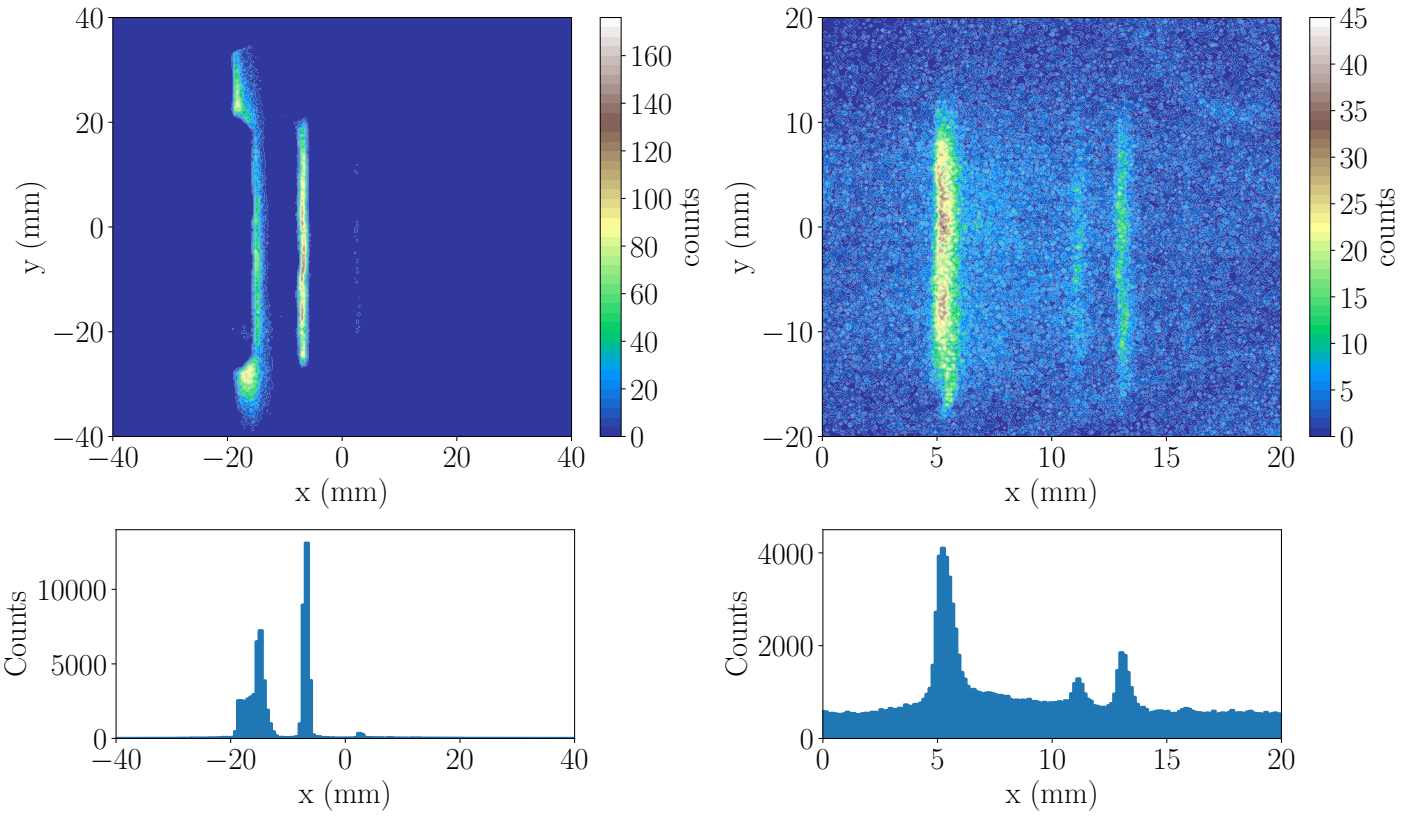

(a) Shadow of the grating plus 0 order light.

(b) 1st and 2nd order lines.

Figure 3.27: 2D images with Mg anode and their respective projections along the x axis (see text).

this, we studied how the intensity and width of the lines varied depending on the position of the grating and the slit. In order to have good statistics and to obtain well-defined high-order lines, long measurements would be needed, but for the present topic ten-minute measurements are long enough. For each measurement, a Gaussian fit is performed to the most intense peak and its height and width are calculated. An example is shown in **Figure 3.28**. The optimal position will be the one with the highest intensity and the narrowest peaks.

We define the different spatial directions in our setup as follows: the z-direction corresponds to the direction of the axes of the vacuum chambers, the x-direction is the one in which the baffle and slit move, i. e. in and out of the chambers, and the y-direction corresponds to up and down, which is not relevant in these tests since the beam is a vertical line. The grating can be moved in all three directions. First, the optimal position of the slit was found, then for the grating in the x and z axes. The results are presented in **Figure 3.29** to **3.31**. These positions are measured using the scales of the linear feedthroughs.

Since the ideal position of the slit may depend on the position of the grating, after these tests the optimal positions were checked again but in the reverse order, getting the same

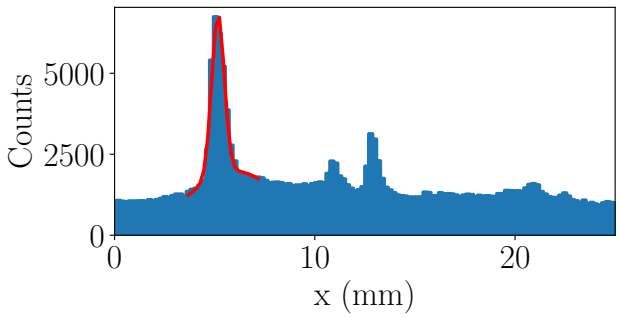

Figure 3.28: Example of a fit to find the optimal position of the grating. The total fit is plotted in red, which is the sum of two Gaussian distributions, one for the peak and one for the background.

results. Therefore, we can state that the optimal position is $x = 17.0$ mm for the slit and $x = 17.75$ mm, $z = 9.0$ mm for the grating. As mentioned above, the y position has no effect due to the symmetry of the system and an intermediate position of $y = 13.15$ mm was chosen. With these settings, the baffle must be placed in $x = 13.00$ mm to correctly block the zero-order light. The feedthrough of the baffle does not have a scale so the position is measured by the length of the screw.

Finally, we studied whether rotating the grating could further improve the quality of the spectra. The feedthrough allows us to tilt it in both the XZ and XY plane using two micrometer screws. Due to the way the rotation mechanism works, the grating also moves so it has to be positioned again in its optimal position. The corrections that must be applied in each case have been calculated and are listed in **Table 3.2** and **Table 3.3**. The results of the measurements are shown in **Figure 3.32** and **Figure 3.33**. They prove that it is better not to rotate the grating.

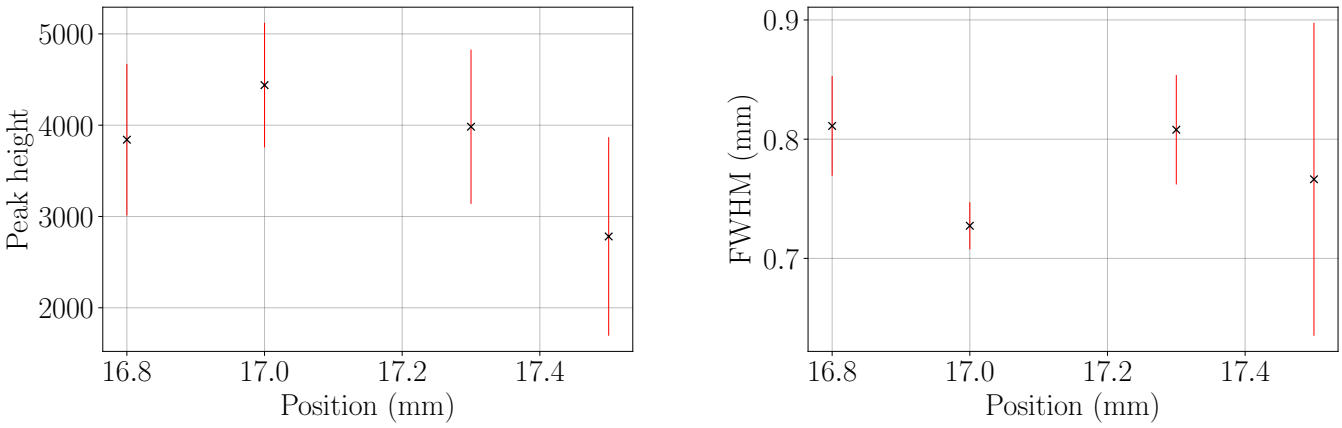

Figure 3.29: Results of the slit measurements. The optimal position is 17.0 mm.

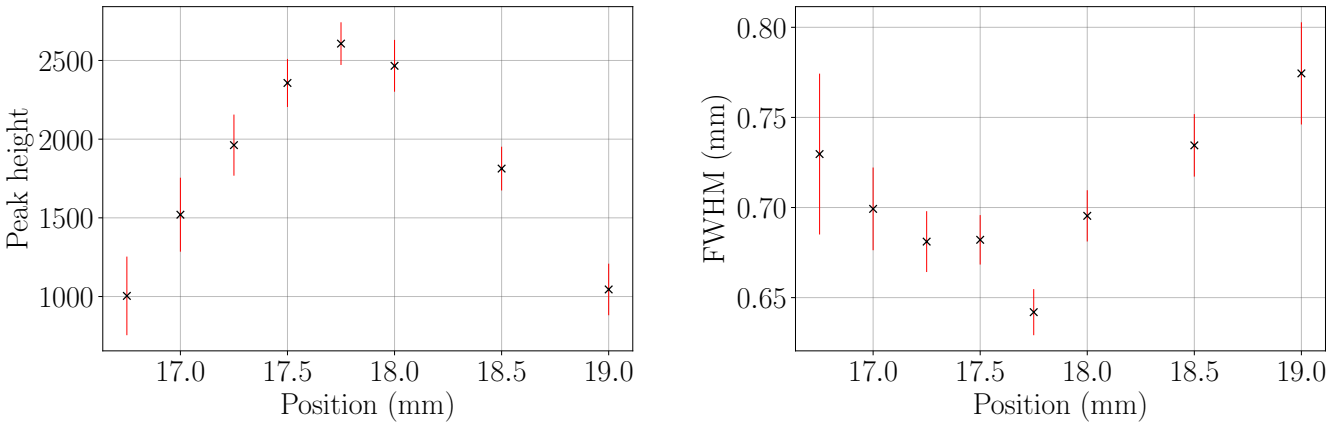

Figure 3.30: Results of the grating measurements (x-direction). The optimal position is 17.75 mm.

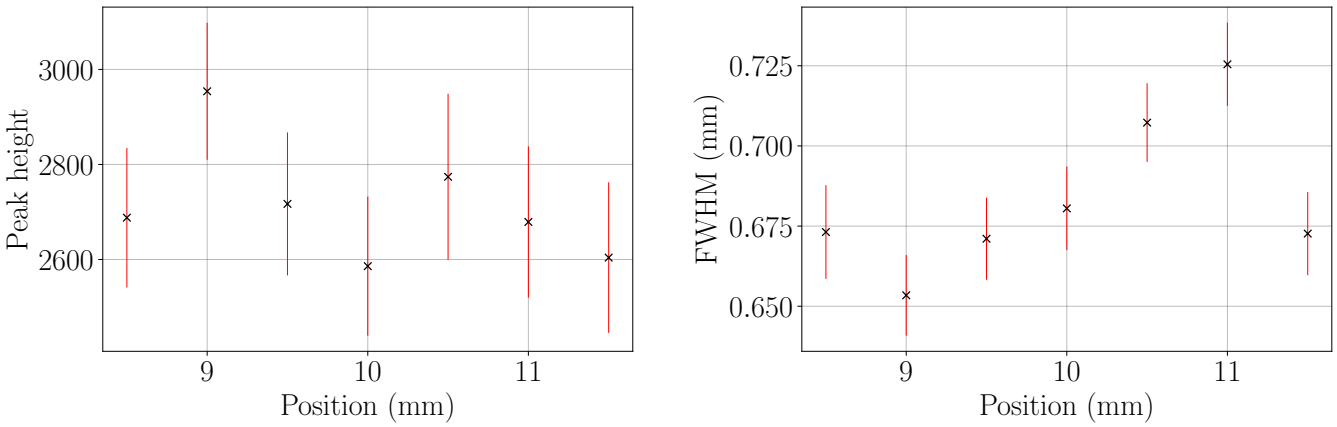

Figure 3.31: Results of the grating measurements (z-direction). The optimal position is 9.0 mm.

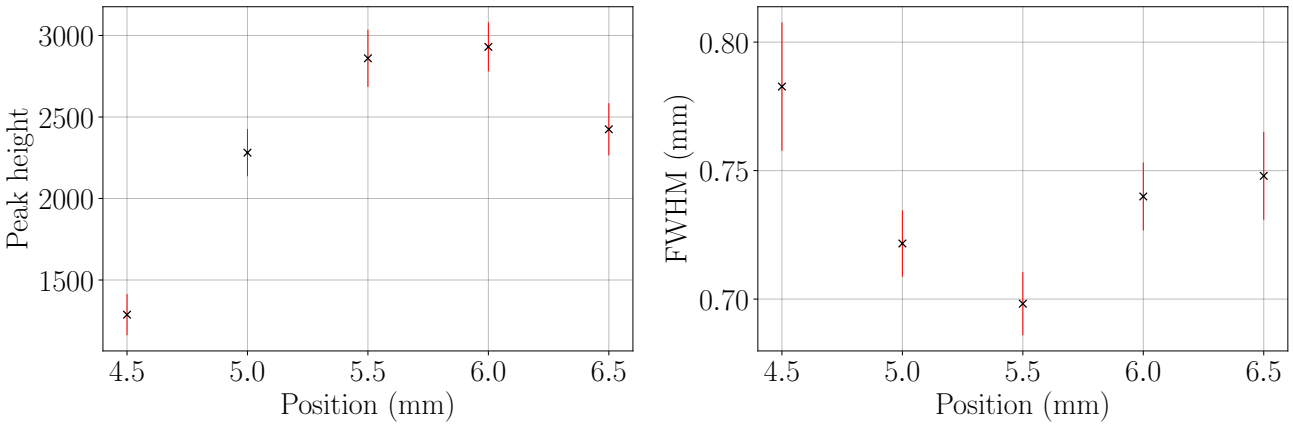

Figure 3.32: Results of the grating measurements (tilting XZ plane). The optimal position of the corresponding micrometer screw is 5.5 mm, which was the original position (no tilting).

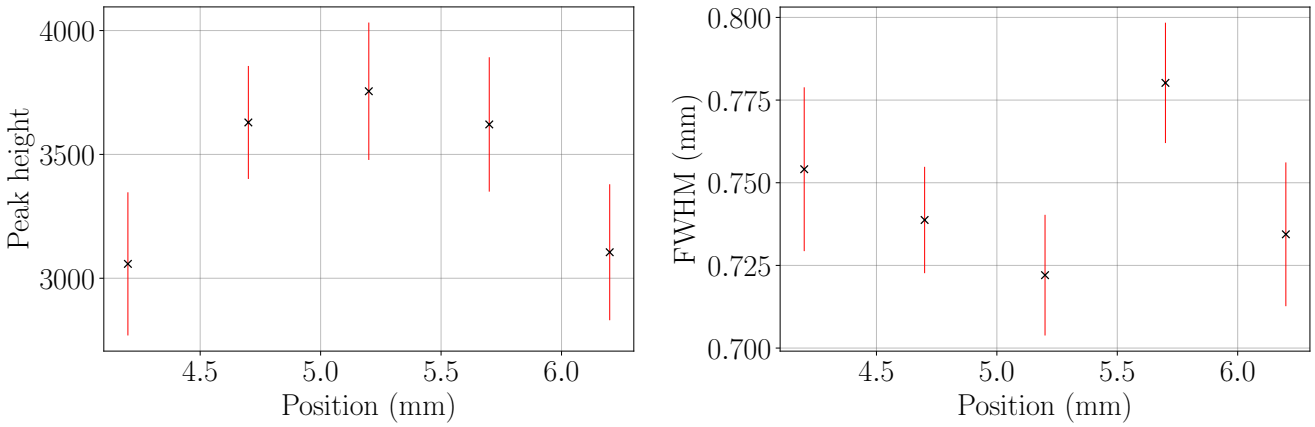

Figure 3.33: Results of the grating measurements (tilting XY plane). The optimal position of the corresponding micrometer screw is 5.2 mm, which was the original position (no tilting).

Position	x change	z change
4.5	−0.96	−3.14
5.0	−0.47	−1.57
5.5	0	0
6.0	0.47	1.57
6.5	0.93	3.13

Table 3.2: Corrections to the grating position when rotating in the XZ plane.

Position	x change	y change
4.2	0	−3.14
4.7	0	−1.57
5.2	0	0
5.7	0	1.57
6.2	0	3.14

Table 3.3: Corrections to the grating position when rotating in the XY plane. The change in x is negligible.

3.5 Wavelength calibration and spectra acquisition

With all the components placed in their optimal positions, finally everything is set up for the acquisition of energy-resolved spectra. Before performing the energy calibration, a way of subtracting the background was explored, since it is relatively high for the previously obtained spectra. Indeed, as it can be seen in **Figure 3.34a**, several "hot spots" are present in our spectra. However, when the x-ray source is turned off, a uniformly distributed, low-intensity background is observed. Therefore, it was concluded that the observed hot-spots had to be related to the x-ray source. To verify this, we completely closed the slit and

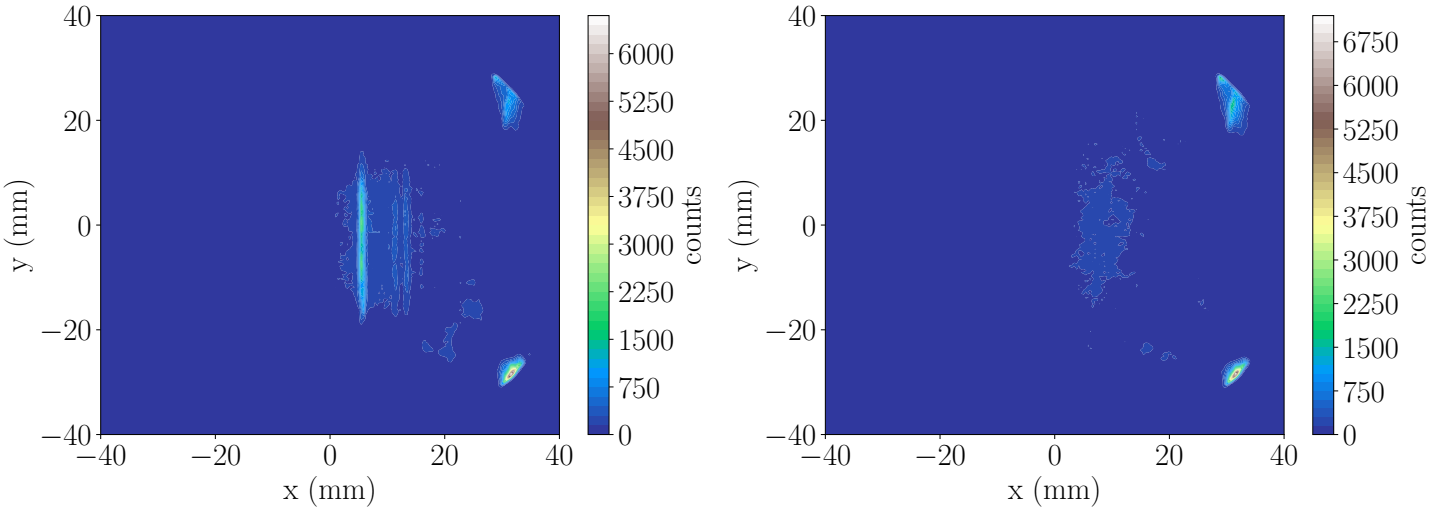

(a) Mg lines plus background.

(b) Background.

Figure 3.34: 2D images with Mg anode showing spectral lines and background. In the first image, the slit was set to 0.3 mm width, while in the second image it is completely closed. Both measurements are one hour long.

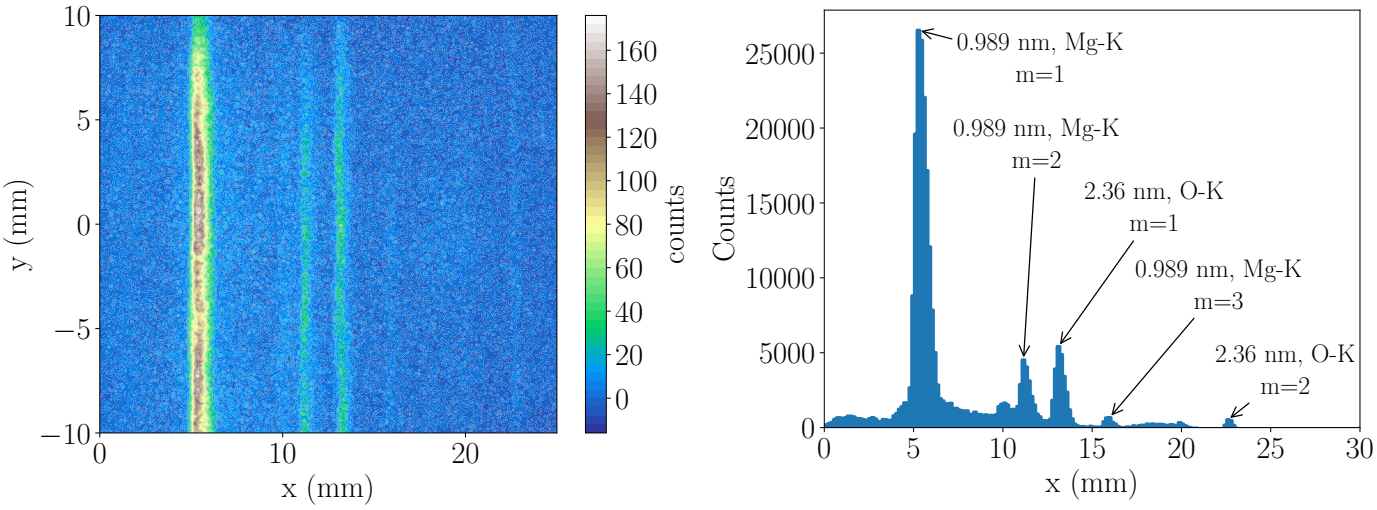

(a) 2D spectrum.

(b) Projection on the x-axis.

Figure 3.35: Mg spectrum with subtracted background.

conducted a measurement with the x-ray source turned on. This way, the beam is not able to reach the grating and the detector, but background radiation does. The outcome is shown in **Figure 3.34b** and one can see that it is exactly what has to be subtracted from the other spectrum to suppress the background contribution. These high background spots probably appear due to photons reaching the detector after being reflected inside the chamber.

In order to calibrate the spectrometer, the background was subtracted from the measurement with opened slit. The resulting 2D image in the central region of the detector and its projection are displayed in **Figure 3.35**, along with labels for the peaks that we could identify. The wavelengths of the x-ray lines have been taken from the x-ray data booklet [32]. Using the center positions of the five peaks labeled in **Figure 3.35b** we can find the relationship between the wavelength of a photon, λ, and its position on the detector, x. Starting from the grating equation **(2.14)**, we have

$$\lambda = \frac{\sin\alpha + \sin\beta}{N} \ . \tag{3.3}$$

Here, m is set to 1 since we are treating second-order light as first-order but with twice the wavelength. By looking at **Figure 3.2**, it follows that the relationship between the diffraction angle β and the impact position x is

$$\beta = \arctan\left(\frac{x}{r_i'}\right) - \frac{\pi}{2} \ , \tag{3.4}$$

where r_i' is the distance grating-detector. The values of α, N, and r_i' can be found in the

grating specifications (**Table 3.1**). To perform the fit, two parameters were added to the equation: an offset C and a scale factor K. Thus, the fit formula is

$$\lambda\ [\text{nm}] = \frac{\sin(88.6) + \sin\left(\arctan\left(\frac{(x\ [\text{mm}]\ + C)\cdot K}{235}\right) - 90\right)}{0.0024}\ . \tag{3.5}$$

The fit was applied to our five data points, giving the values $K = 1.087 \pm 0.004$ and $C = 10.53 \pm 0.10$. This is shown in **Figure 3.36**.

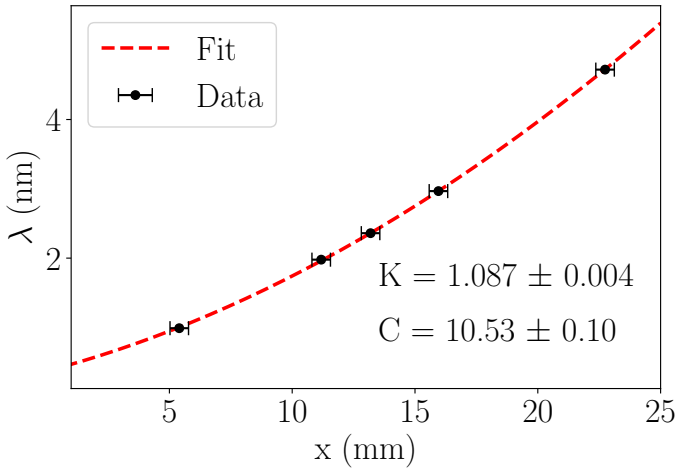

Figure 3.36: Calibration curve.

This finally allows us to achieve the main goal of this work: to obtain energy-calibrated spectra using our test setup. **Figure 3.37** shows one spectrum acquired using the magnesium anode, and **Figure 3.38** shows one obtained using the inner part of a euro coin as the anode, which is made of 75% copper and 25% nickel [33]. At last, in order to explain the lower intensity, continuous part of these spectra, the bremsstrahlung contribution was calculated using Kramer's law **(2.7)** and taking into account higher diffraction orders plus the filter foil transmission. It is plotted along with the spectra in **Figure 3.39** and **Figure 3.40**. As one can see, it fits reasonably well to the obtained spectra shape.

As a final remark, the spectral resolution of our setup can be estimated using the Mg-K, m = 1 line in **Figure 3.37**. The FWHM of this peak is 0.1210 ± 0.0007 nm, which gives a resolution of $\frac{\text{FWHM}}{\lambda} \approx 12\%$ at 1 nm. The McPherson 251MX spectrometer, on which our test setup is based, achieves a spectral resolution of about 1.4% [34]. There are two main reasons why we cannot reach such a good resolution. First, our position resolution is not optimal and can be improved by using Constant Fraction Discriminators for the delay line signals. Second, the 251 MX uses a 20 µm-wide slit, while ours is 300 µm wide. In our

setup all components are manually adjusted, so performing tests with different slit widths is very time consuming, since it requires to vent, open the vacuum chambers, change the slit width and pump again (note that the pumping and venting must be done very slowly to avoid breaking the filter foil). In addition, tests with such small slits would require much longer measurements to have good intensities. Both aspects can be improved in the future to achieve a more accurate spectrometer.

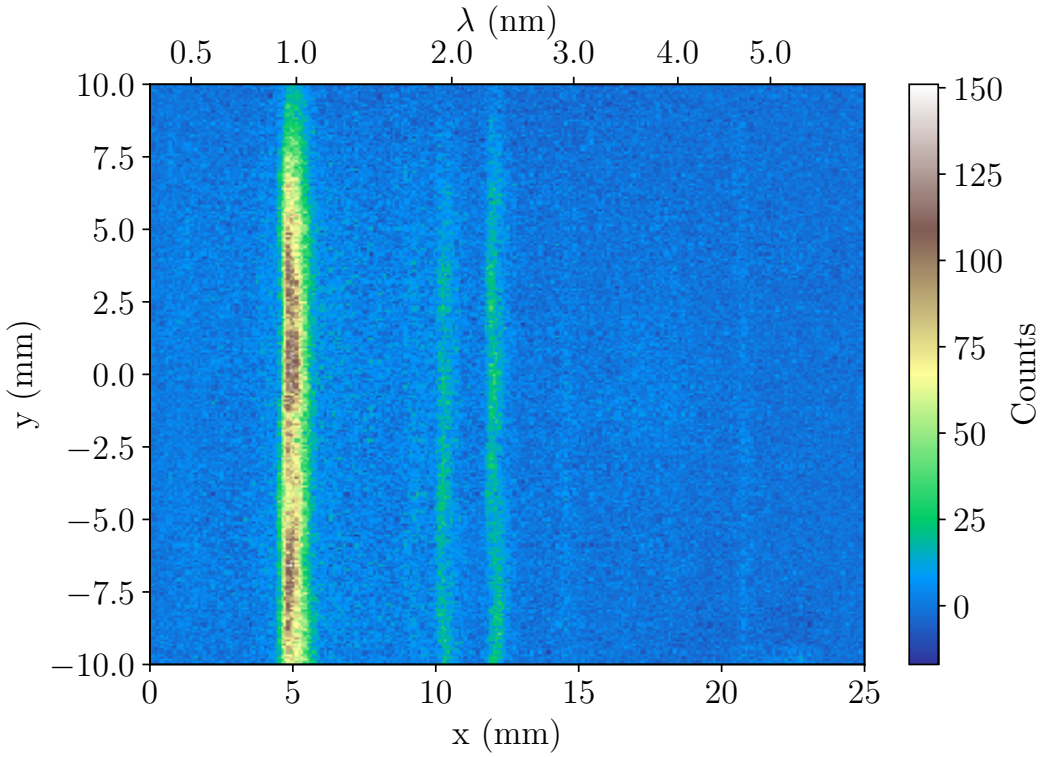

(a) 2D spectrum.

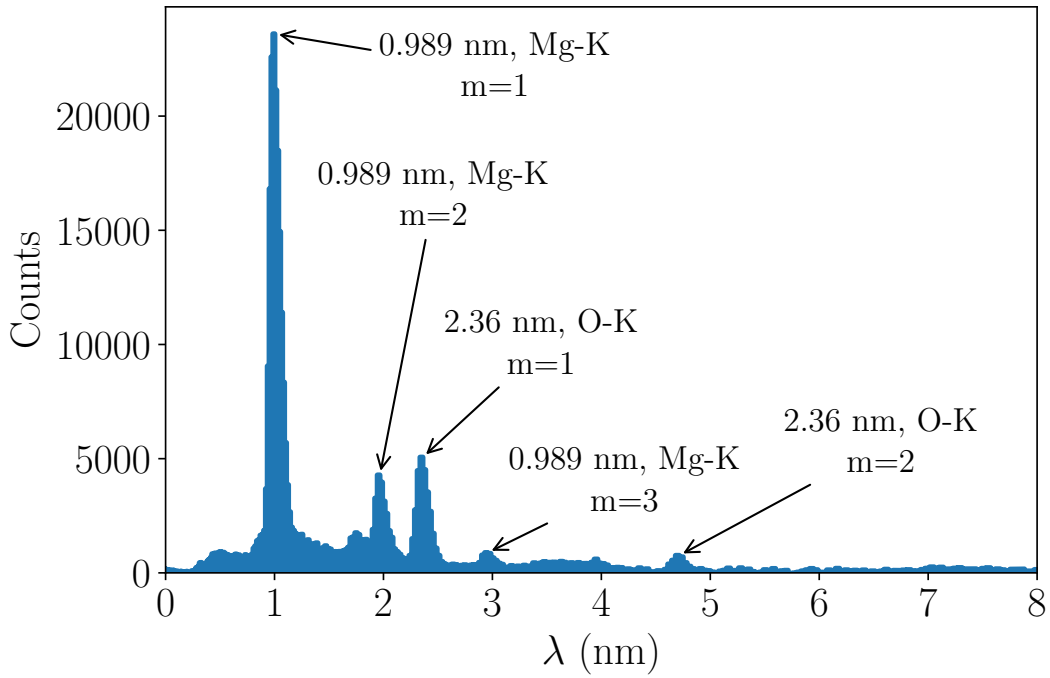

(b) 1D spectrum (projection).

Figure 3.37: Mg calibrated spectrum.

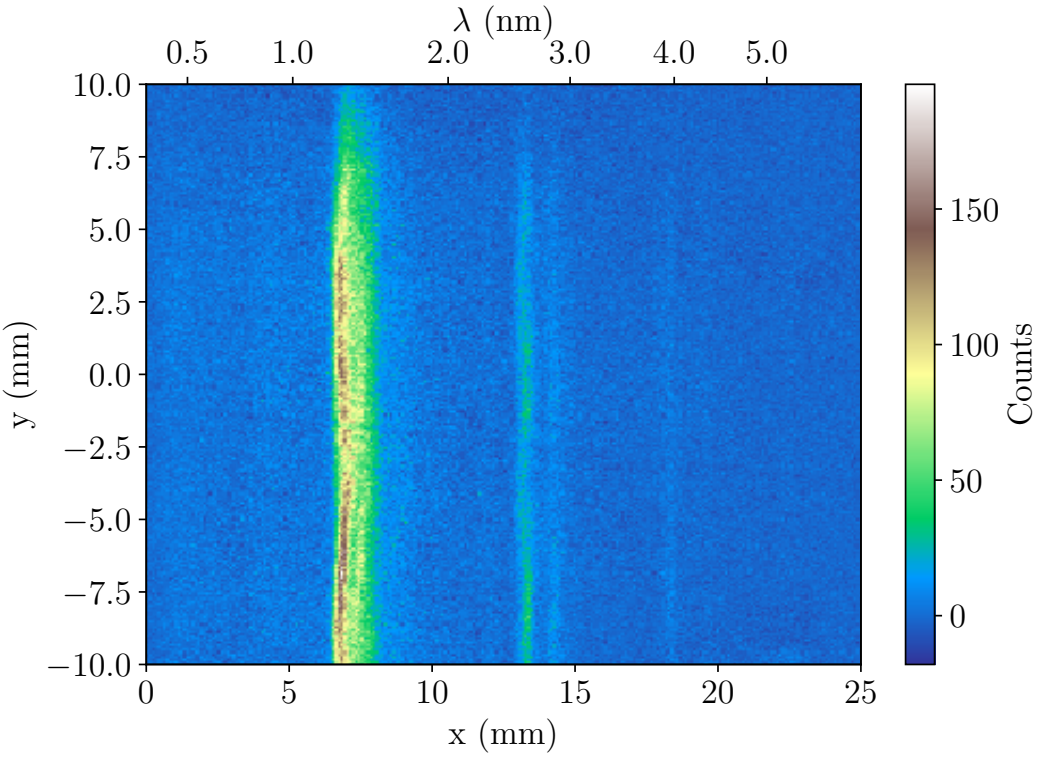

(a) 2D spectrum.

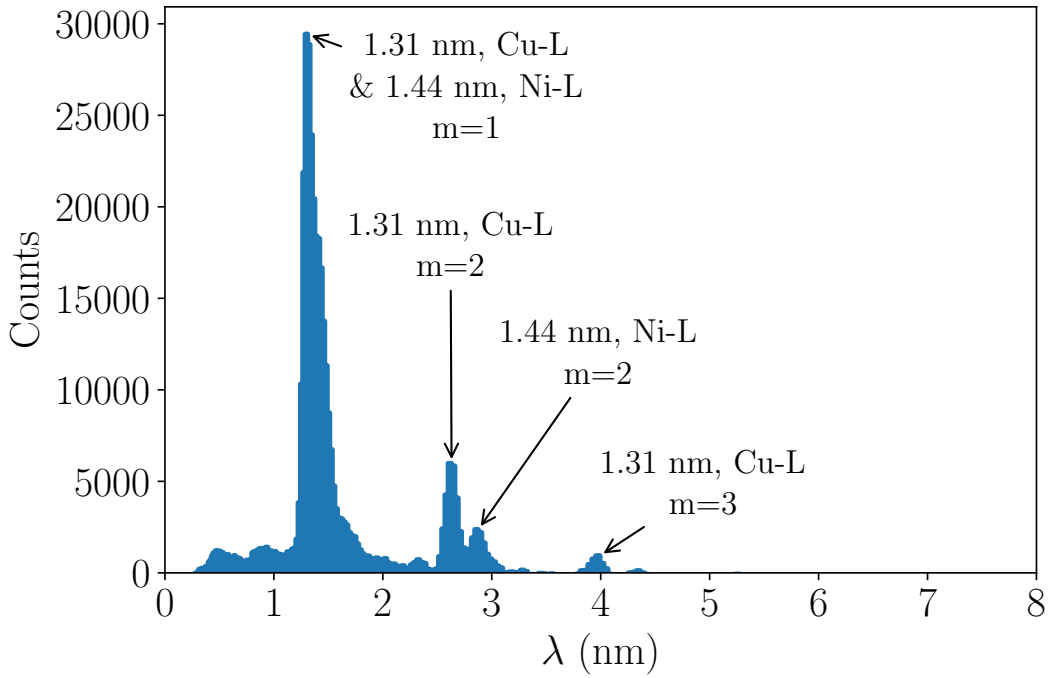

(b) 1D spectrum (projection).

Figure 3.38: CuNi calibrated spectrum.

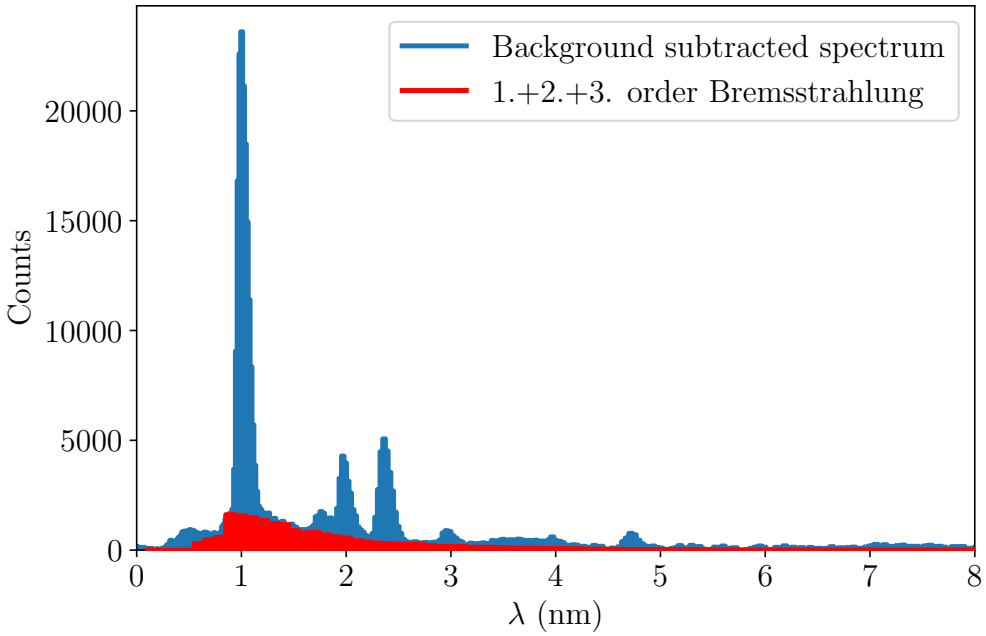

Figure 3.39: Mg calibrated spectrum with bremsstrahlung.

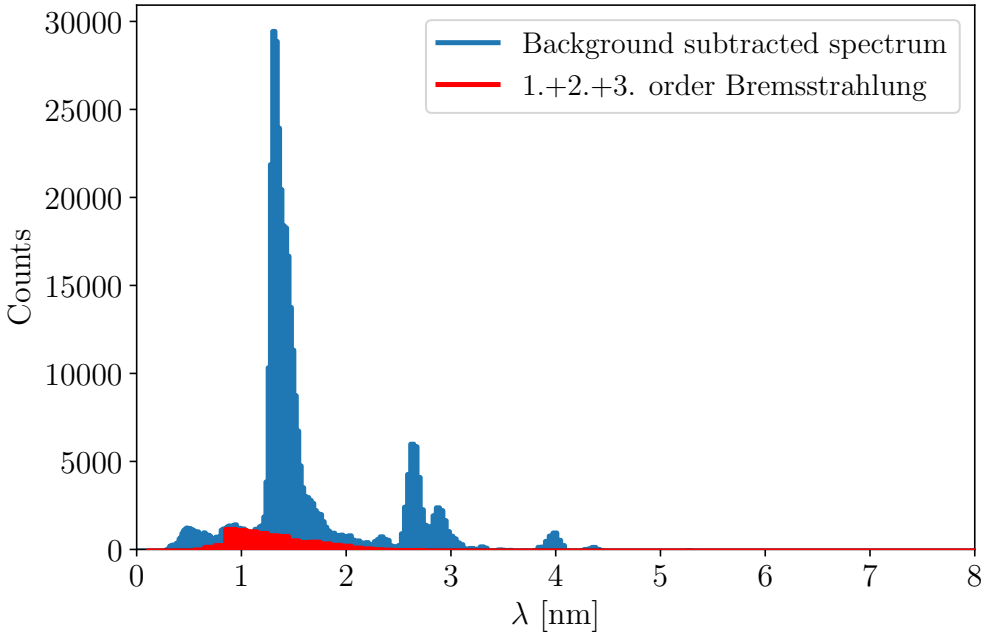

Figure 3.40: CuNi calibrated spectrum with bremsstrahlung.

Chapter 4

Conclusion and outlook

The fluorescence detector desired in the laser cooling area of the upcoming SIS100 at GSI/FAIR has been designed to meet the requested requirements: fast time response, sufficient efficiency in the XUV and soft x-ray region, and an energy-resolved detection. This is achieved by combining an MCP detector with a delay line anode, which allows us to know the position of the detected photons. By adding a diffraction grating, the incident beam is split according to its wavelengths, which in our setup means an energy-resolved spectrum.

A brief theoretical background has been presented so that the variables that can affect the performance of the spectrometer are known and can be studied in the future. A test setup, using an MCP from the former WITCH experiment, has been built in Münster. Its position sensitivity and time response has been studied, demonstrating that such a setup fulfills the conditions to be used in the laser cooling system of SIS100. Lastly, the position of the diffraction grating and the entrance slit has been optimized so that the spectra have well-defined peaks, and the setup is calibrated in order to achieve an energy-resolving detection. As a main result of the thesis, two spectra are presented: one using a magnesium anode and one using a copper-nickel anode. The spectral resolution and limitations of the current test setup have been discussed. This concludes the work, showing that our test setup is capable of detecting the energy of the incident x-ray photons.

Presently, the setup is being upgraded so that the spectrometer that will finally be in FAIR has the best possible performance and quality. A new MCP detector, with the option to use a coated front channel plate for increased quantum efficiency, is already being studied in the *Institut für Kernphysik* in Münster. In addition, the replacement of the Leading Edge Discriminators within our setup with Constant Fraction Discriminators is underway, which will allow for a better position and time resolution. Automation of all the components is also necessary since a manual adjustment is not possible during the operation of a particle accelerator. These enhancements are outside the scope of this thesis but will be presented in the near future in the Ph. D. dissertation of Ken Ueberholz.

Appendix A

Technical drawings (by Christian Huhmann)

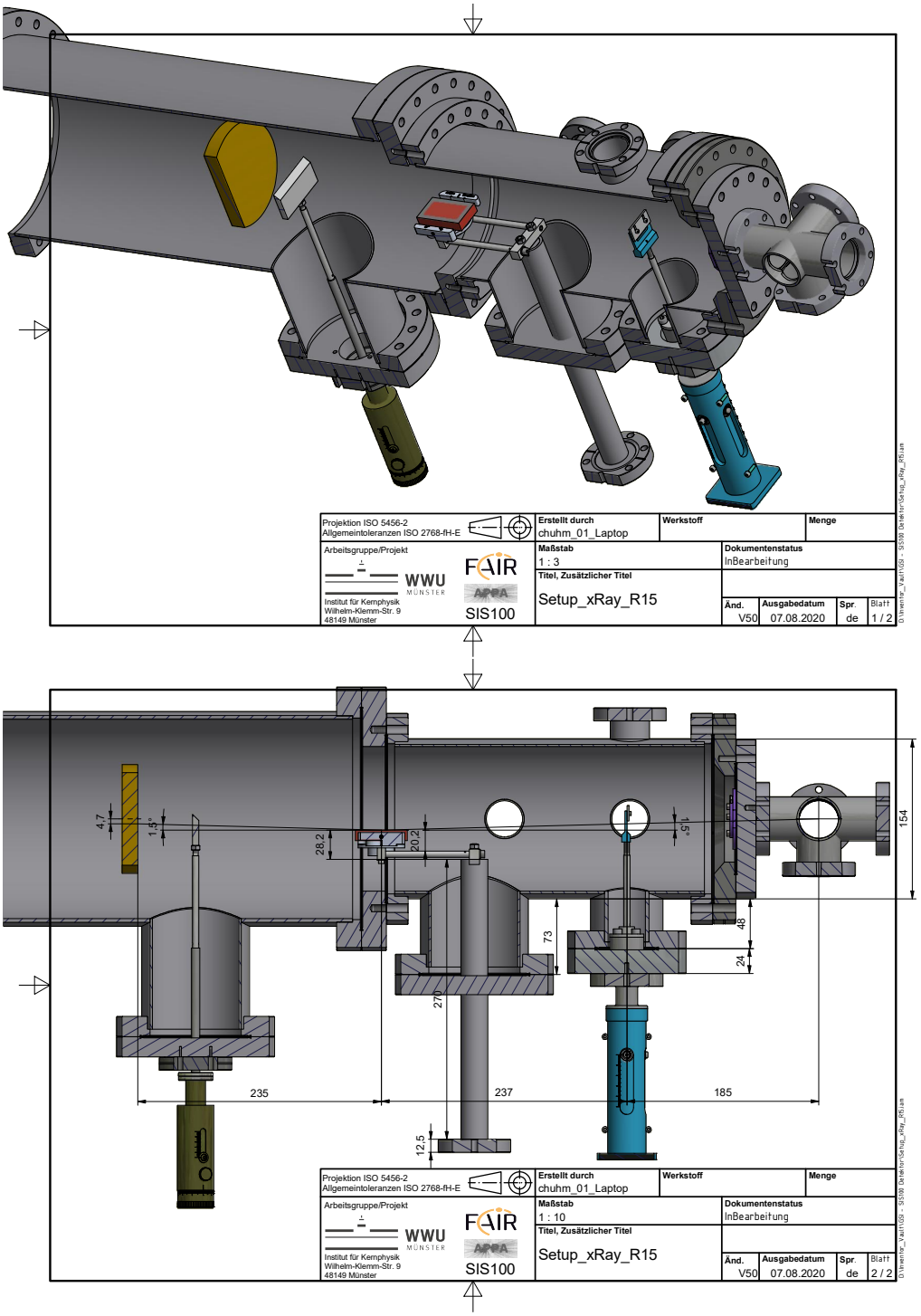

Figure A.1: Technical drawing of the test setup.

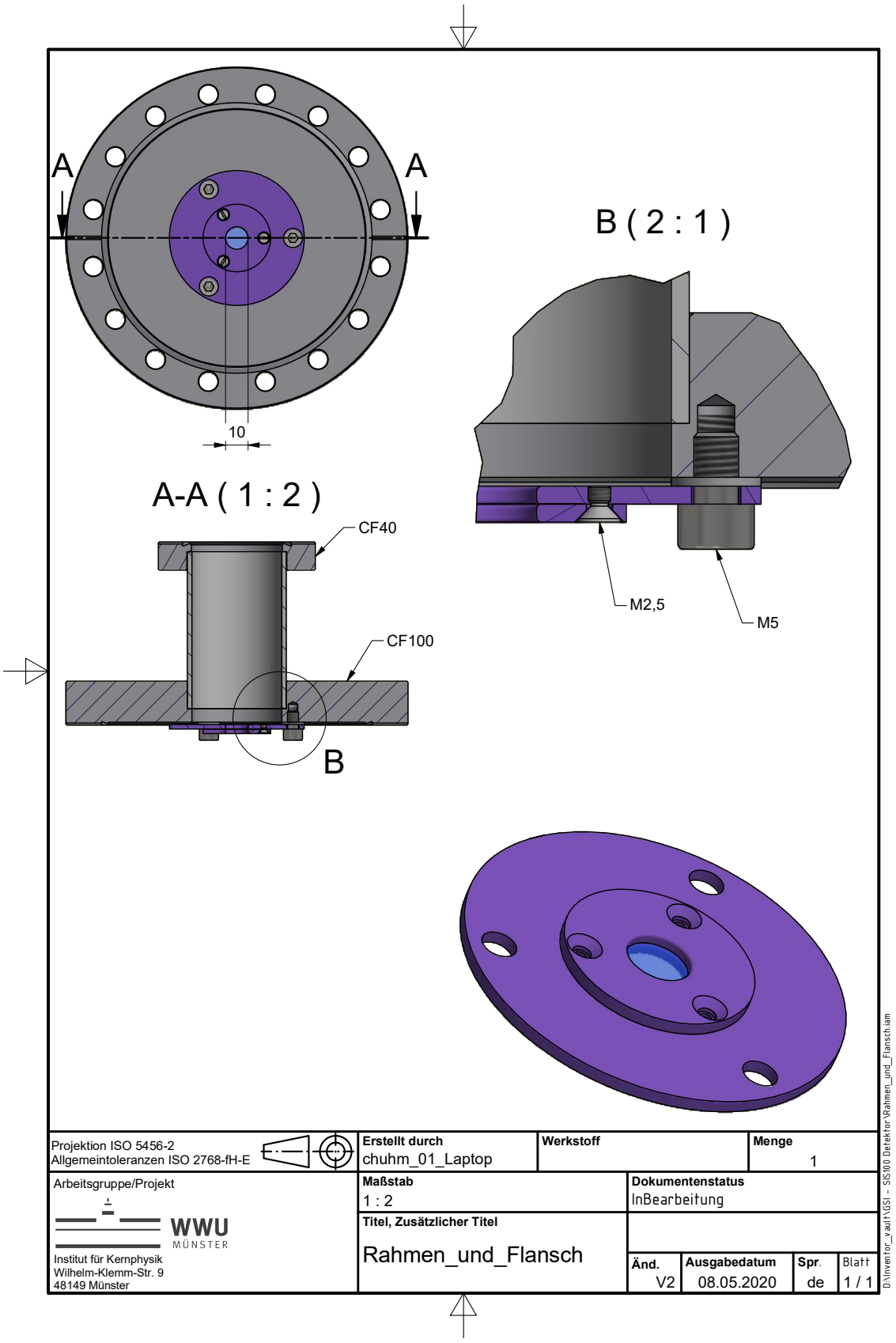

Figure A.2: Technical drawing of the filter foil mounting frame.

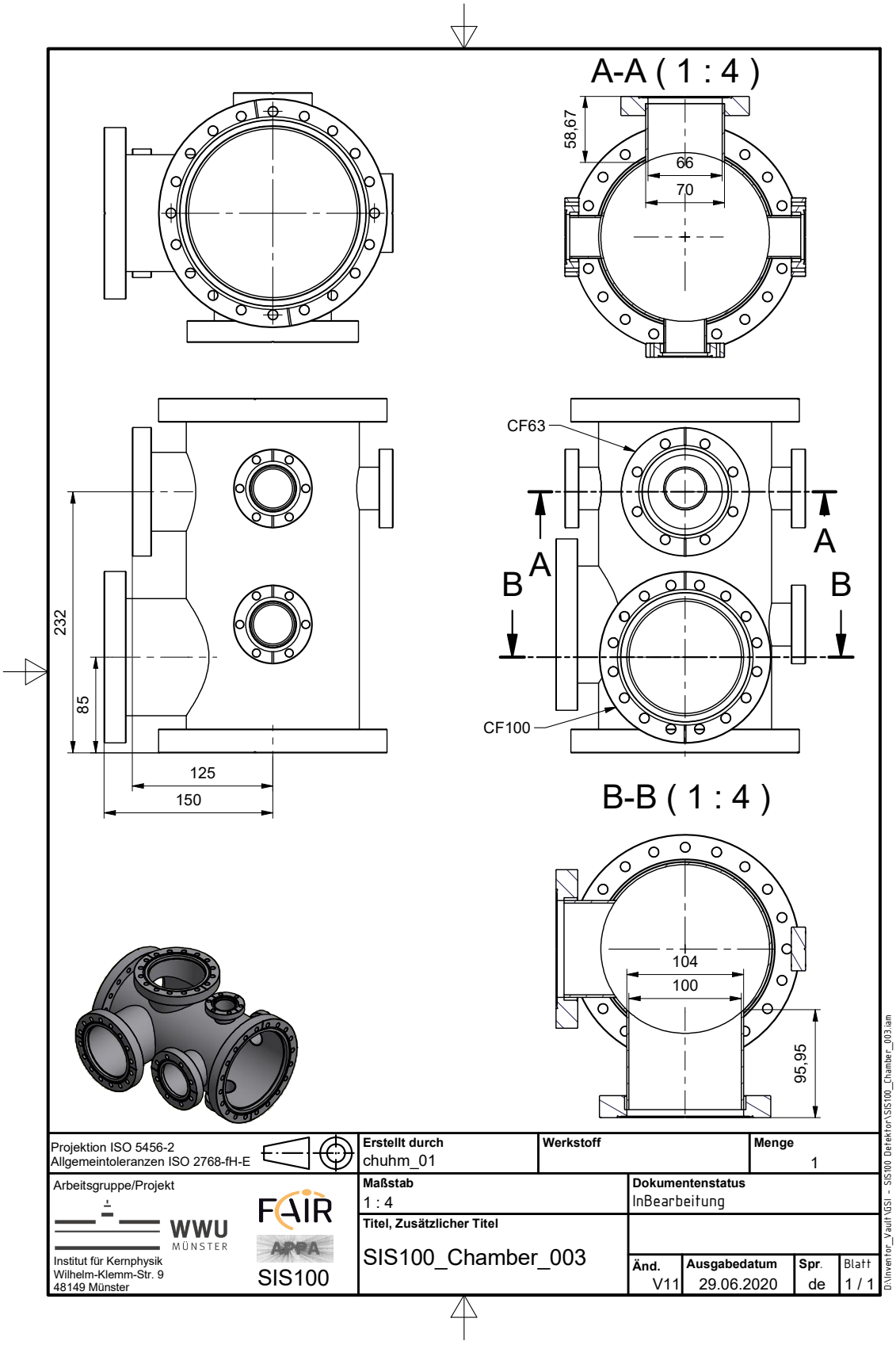

Figure A.3: Technical drawing of the grating vacuum chamber.

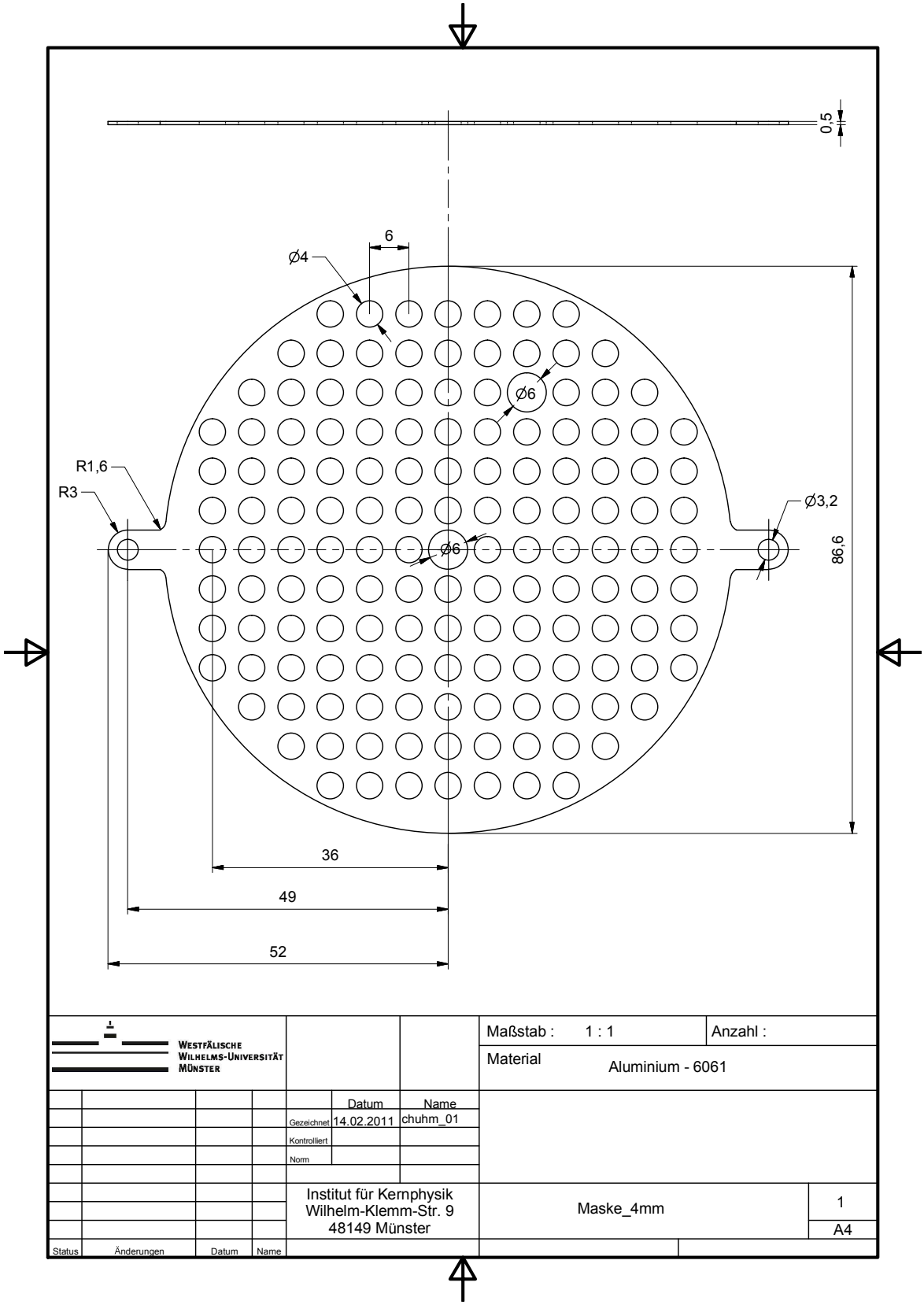

Figure A.4: Technical drawing of the aperture mask used in the position calibration.

List of Figures

List of Tables

Bibliography

[1] GSI & FAIR webpage, `https://www.gsi.de/en/researchaccelerators/fair.htm`, accessed: 26.10.2020.

[2] APPA webpage, `https://www.gsi.de/en/researchaccelerators/fair/research/appa_from_atoms_and_planets_to_cancer_treatment.htm`, accessed: 27.10.2020.

[3] U. Schramm *et al.*, "Laser cooling of relativistic heavy ion beams," in *Proceedings of the 2005 Particle Accelerator Conference*, 2005, pp. 401–403.

[4] D. Winters *et al.*, "Laser cooling of relativistic highly charged ions at FAIR," in *7th International Particle Accelerator Conference*, May 2016, p. 3747.

[5] H. Poth, "Electron cooling: theory, experiment, application," *Physics reports*, vol. 196, no. 3-4, pp. 135–297, November 1990.

[6] S. van der Meer, "Stochastic damping of betatron oscillations in the ISR," CERN, Geneva, Tech. Rep. CERN-ISR-PO-72-31, August 1972.

[7] J. Marriner and D. McGinnis, "An introduction to stochastic cooling," in *AIP Conference Proceedings*, vol. 249, no. 1, 1992, pp. 693–761.

[8] L. Eidam *et al.*, "Cooling rates and intensity limitations for laser-cooled ions at relativistic energies," *Nuclear Instruments and Methods in Physics Research (A)*, vol. 887, pp. 102–113, April 2018.

[9] W. D. Phillips, "Nobel Lecture: Laser cooling and trapping of neutral atoms," *Reviews of Modern Physics*, vol. 70, no. 3, pp. 721–741, July 1998.

[10] J. Hangst *et al.*, "Laser cooling of a bunched beam in a synchrotron storage ring," *Physical Review Letters*, vol. 74, no. 22, p. 4432, May 1995.

[11] D. Winters *et al.*, "Laser cooling of relativistic heavy-ion beams for FAIR," *Physica Scripta*, vol. 2015, no. T166, p. 014048, November 2015.

[12] D. Laguitton and W. Parrish, "Experimental spectral distribution versus kramers' law for quantitative x-ray fluorescence by the fundamental parameters method," *X-Ray Spectrometry*, vol. 6, no. 4, pp. 201–203, October 1977.

[13] J. Singh, "Characteristic and continuous x-rays," `https://www.concepts-of-physics.com`, accessed: 26.01.2021.

[14] G. F. Knoll, *Radiation detection and measurement*, 3rd ed. John Wiley & Sons, 1999.

[15] C. Schroer and B. Lengeler, *X-ray optics*. Springer New York, 2007, pp. 1153–1164.

[16] E. Spiller, *Soft X-ray optics*. SPIE press, 1994.

[17] Hamamatsu Photonics K.K., *MCP Assembly Guide*, September 2006.

[18] J. L. Wiza, "Microchannel plate detectors," *Nuclear Instruments and Methods*, vol. 162, no. 1, pp. 587–601, June 1979.

[19] M. Lampton, "The microchannel image intensifier," *Scientific American*, vol. 245, pp. 62–71, November 1981.

[20] G. W. Fraser, "The soft x-ray quantum detection efficiency of microchannel plates," *Nuclear Instruments and Methods in Physics Research*, vol. 195, no. 3, pp. 523–538, April 1982.

[21] C. Martin and S. Bowyer, "Quantum efficiency of opaque CsI photocathodes with channel electron multiplier arrays in the extreme and far ultraviolet," *Applied Optics*, vol. 21, no. 23, pp. 4206–4207, December 1982.

[22] G. W. Fraser *et al.*, "The soft x-ray detection efficiency of coated microchannel plates," *Nuclear Instruments and Methods in Physics Research*, vol. 224, no. 1, pp. 272–286, July 1984.

[23] O. Siegmund, J. Vallerga, and A. Tremsin, "Characterization of microchannel plate quantum efficiency," in *Proceedings of SPIE: UV, X-Ray, and Gamma-Ray Space Instrumentation for Astronomy XIV*, vol. 5898, 2005, pp. 113–123.

[24] G. B. Andresen, ALPHA Collaboration *et al.*, "Antiproton, positron, and electron imaging with a microchannel plate/phosphor detector," *Review of Scientific Instruments*, vol. 80, no. 12, p. 123701, December 2009.

[25] M. P. Sinha and M. Wadsworth, "Miniature focal plane mass spectrometer with 1000-pixel modified-CCD detector array for direct ion measurement," *Review of Scientific Instruments*, vol. 76, no. 2, p. 025103, February 2005.

[26] R. H. Brigham *et al.*, "Characterization of two resistive anode encoder position sensitive detectors for use in ion microscopy," *Review of Scientific Instruments*, vol. 64, no. 2, pp. 420–429, February 1993.

[27] Shimadzu Corporation, *Shimadzu Diffraction Gratings*, 6th ed.

[28] C. Palmer and E. Loewen, *Diffraction grating handbook*, 6th ed. Newport Corporation, 2005.

[29] P. Friedag, "Setup and calibration of a position sensitive microchannel plate detector and analysis of a test run optimizing the WITCH experiment," Ph.D. dissertation, WWU Münster, June 2013.

[30] CXRO database, `https://henke.lbl.gov/optical_constants/filter2.html`, accessed: 30.11.2020.

[31] Lebow Company webpage, `https://lebowcompany.com/about-foils-2`, accessed: 30.11.2020.

[32] A. C. Thompson and D. Vaughan, *X-ray data booklet*, 3rd ed. Lawrence Berkeley National Laboratory, September 2009.

[33] Copper Development Association, `https://copperalliance.org.uk/about-copper/applications/coinage/copper-euro/`, accessed: 12.12.2020.

[34] McPherson Inc, *McPherson Model 251MX Data Sheet.*